ABSTRACT

FLOW CHARACTERIZATION AND STABILITY ANALYSIS IN RECTANGULAR LID-DRIVEN CAVITIES WITH PARTICLE SUSPENSIONS

Abhishek Sunkavalli, MS
Department of Mechanical Engineering
Northern Illinois University, 2017
John Shelton, Director

The lid-driven cavity is a canonical problem in the field of analytical and computational fluid dynamics where a system is comprised of a square domain of an incompressible fluid, its upper lid has a specified velocity and the remaining wall boundaries are subjected to fixed, no-slip, zero-velocity constraints. There are numerous examples found in the literature that address the validation of the system's well-known, stable behavior, which includes a primary recirculating vortex, secondary corner vortices, and a velocity profile through the center midpoint y-axis that is shown to be dependent on the Reynolds number. By increasing the cavity depth to aspect ratios of 1x1.5, other studies have suggested that a different kind of stable fluid structure develops, which includes a primary recirculating vortex, secondary corner vortices, and a new secondary recirculating vortex that developed from the corner vortices of the square cavity and merged together at the bottom of this rectangular system. Mathematical perturbations to the square lid-driven cavity problem have been shown to decrease the stability of the flow structure and exhibit 3D, turbulent flow characteristics. Particle suspensions could be used as physical representations of these mathematical perturbations. In this thesis, I will investigate how these physical perturbations affect the stable flow characteristics observed in lid-driven cavities with high aspect ratios. The base flow is two-dimensional and is computed numerically over a range of Reynolds numbers and is perturbed with varying volume fractions and types of particle

suspension. Using Ergun-Wen-Yu drag and particle slip velocities are used to represent particle-fluid interactions. In this investigation, open-source CFD software called OpenFOAM will be used to solve the Navier-Stokes equations for the fluid phase and particle-particle interactions for the solid phase. The purpose of these studies and analyses will aid in the future findings of advantageous methodologies to determine the flow characterization of drilling mud.

NORTHERN ILLINOIS UNIVERSITY
DE KALB, ILLINOIS

AUGUST 2017

FLOW CHARACTERIZATION AND STABILITY ANALYSIS IN RECTANGULAR LID-DRIVEN CAVITIES WITH PARTICLE SUSPENSIONS

BY

ABHISHEK SUNKAVALLI

A THESIS SUBMITTED TO THE GRADUATE SCHOOL

IN PARTIAL FULFILLMENT OF THE REQUIREMENTS

FOR THE DEGREE

MASTER OF SCIENCE

DEPARTMENT OF MECHANICAL ENGINEERING

Thesis Director:
John Shelton

ACKNOWLEDGEMENTS

It gives me immense pleasure to thank my advisor Dr.John Shelton who guided me in each and every step to complete this thesis work. He supported me in regards to research and scholarship right from beginning of this thesis. His great attitude towards work made me work comfortably without any hassle. I would also like to thank my committee members Dr. Nicholas Pohlman and Dr. Jenn Tern Gau who actively took time and gave some valuable comments to improve my thesis work.

I would like to thank Dr. Pradip Majumdar who encouraged me and supported me during my hardships.

Last but not the least, I would like to thank my parents, my sister and brother-in-law whose love and support motivated me for completing my Master's degree and thesis.

TABLE OF CONTENTS

Page

LIST OF TABLES

Page

LIST OF FIGURES

Page

Page

Page

Page

1. INTRODUCTION

With so much of Industrial revolution influencing the areas of research, scientists and engineers started developing keen interest and trying to understand the characteristics of flows with more than one phase that i.e. they started to understand and analyze multi-phase flows ; In this thesis we will be analyzing solid-gas flows. To mention a few industrial applications, gas-solid interactions are important in fluidized beds, propulsion and combustions, mixing, medical fields. With advancement in Computational Fluid Dynamics tools to understand the flows coupled with increased capacity of systems to handle complicated simulations eased the way to research on multiphase flows. Even though there has been a quite advancement in the ways the most standard approach is still a system with square cavity with a moving lid is used to analyze the complex fluid flow characteristics. This standard system is named LID DRIVEN CAVITY.

The lid-driven cavity problem has long been used a test or validation case for new codes or new solution methods. The problem geometry is simple and two-dimensional, and the boundary conditions are also simple.

The standard case is fluid contained in a square domain with Dirichlet boundary conditions on all sides, with three stationary sides and one moving side. One of the pioneering works on this flow is the work done by Ghia et al [10]. for a two-dimensional case. Using the stream function-vorticity formulation of the Navier-Stokes equations, results were obtained for the flow at various Reynolds numbers ranging from 100-10,000.

The main reasons for considering lid driven cavity is for its robust domain yet able to produce the most trivial and complicated flow characteristics. Extensive research has been done using lid driven cavity through decades which resulted in enormous references to look at and compare, validate the system and domains. Standard square lid driven cavity is said to show a primary vortex, up-stream and down-stream eddies. With increase in the Reynolds numbers the sizes of the up-stream and down-stream eddies change and also we can clearly see a shift in the center of the primary vortex.

As the geometry of lid driven cavity is very simple, research has been done for different aspect ratios. In some cases the moving lid is replaced by moving fluid forming a new type of situations i.e. shear-driven cavity. Various types of numerical techniques were used to compute the solutions for this problem. Also, this problem can be solved in both laminar and turbulent flow. Because of its simple boundary conditions, compatibility with various numerical approaches and vast literature to compare with, the lid driven cavity has always been of interest, and extensive research is still being done to better understand the flow characteristics.

The main focus of this work was to understand the flow characteristics in the lid driven cavity when its lid is moving at a constant velocity. The main aspect being work is done with lid driven cavities with aspect ratios of 1.5. That is depth of cavity is 1.5 times the width for aspect ratio 1.5. The matter in the domain being both solid and gas. The main idea being behavior of fluid when perturbations are introduced into the systems through particles. This multiphase matter showed a very different behavior when compared to the standard single phase flow characteristics.

First work was done with the square cavity that is the generic lid driven cavity with single phase to validate the system and approach comparing the results to Ghia et al [10]. Later

rectangular lid driven cavities with single phase have been studied and results are compared with Kumar [11].

2. THEORY

2.1 Lid Driven Cavity:

The lid-driven cavity flow is considered as a benchmark problem for the validation of numerical methods and techniques in computational fluid dynamics [8]. The fluid motion in a square or a rectangular box (also known as the lid driven cavity) is induced by the translation of one wall. The geometry of the lid driven cavity is shown in the Figure 2.1 below. It comprises of a rectangular box of which the top wall translates a horizontal velocity U. The walls on left, right and bottom are fixed. These walls are subjected to a boundary condition where its fluid velocity is the no-slip zero velocity. In 3D, all the boundary conditions remain the same for the additional walls and the geometry is extended to z-direction [8].

The Newtonian fluids in rectangular boxes are governed by two dimensionless parameters, namely Reynold's number (Re) and the aspect ratio [8].

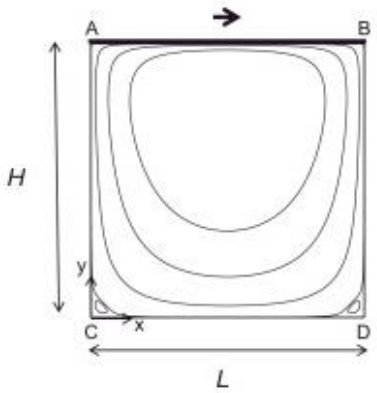

Figure 2.1 Schematic of Lid driven Cavity

The Boundary conditions, for the Lid driven Cavity is as follows [7]:

- No-slip velocity boundary condition u = v = 0 is applied on all the left, right and bottom walls, except the top wall.
- On the top wall u = 1 and v = 0 is applied. The bottom of the cavity is considered as wall.

2.2 Governing Equations:

For an isothermal, incompressible, two-dimensional, Newtonian fluid in lid-driven cavity the laws of conservation of mass and conservation of momentum are considered. The governing non-linear partial differential equations can be written as follows [7].

The continuity equation is given by [7]:

$$\frac{\partial U}{\partial X} + \frac{\partial V}{\partial Y} = 0 \tag{1}$$

The X-Momentum equation is given by [7]:

$$\frac{\partial U}{\partial \tau} + U\frac{\partial U}{\partial X} + V\frac{\partial U}{\partial Y} = -\frac{\partial P}{\partial Y} + \frac{1}{Re}\left[\frac{\partial^2 U}{\partial X^2} + \frac{\partial^2 U}{\partial X^2}\right] \tag{2}$$

The Y-Momentum equation is given by [7]:

$$\frac{\partial V}{\partial \tau} + U\frac{\partial V}{\partial X} + V\frac{\partial V}{\partial Y} = -\frac{\partial P}{\partial Y} + \frac{1}{Re}\left[\frac{\partial^2 V}{\partial X^2} + \frac{\partial^2 V}{\partial X^2}\right] \tag{3}$$

where,

$U = \frac{u}{U_\infty}$ $V = \frac{v}{U_\infty}$ $X = \frac{x}{L}$ $Y = \frac{y}{L}$

$$\tau = \frac{tU_\infty}{L} \qquad P = \frac{p}{\rho U_\infty} \qquad Re = \frac{U_\infty l}{v}$$

2.3 Flow in Lid driven Cavity:

To analyze the flow in the lid driven cavity, it is assumed that it is infinitely long along the transverse direction and the base flow is found to be steady and two-dimensional. In his paper, Ramanan [10], explains the linear stability in a three dimensional lid-driven cavity, by introducing the disturbances. Mathematical perturbation field disturbance is introduced to the pressure and velocity of the base flow. The purpose of this study was to analyze the behavior of the stability critical Reynolds number evolution from 2D and 3D [10].

2.3.1 Navier- Stokes Equation:

According to Ramanan [9], the Navier-Stokes equation are written as:

$$\nabla . \mathbf{u} = \mathbf{0} \tag{4}$$

$$\mathbf{u}_{,t} + \mathbf{u} \cdot \nabla \mathbf{u} = -\nabla p + \frac{1}{Re} \nabla^2 \mathbf{u} \tag{5}$$

where,

∇ = gradient operator,

u = velocity,

p = pressure,

t = time,

Re = Reynolds number,

p = kinematic pressure and

a comma indicates differentiation.

2.3.2 Base Flow

The base flow stability is examined in 2D for an infinitely long cavity in z direction and the equations are given as follows [9]:

$$\nabla . \mathbf{U} = \mathbf{0} \tag{6}$$

$$\mathbf{U} \cdot \nabla_* \mathbf{U} = -\boldsymbol{\nabla}_* \mathbf{P} + \frac{1}{Re} \nabla_*^2 \mathbf{U} \tag{7}$$

where,

∇_* = two-dimensional gradient operator,

U = *base* flow velocity,

P = base flow pressure,

The boundary conditions for the equations (6) and (7) are:

U = (1, 0), at y = 1,

U = (0, 0), at x = 0, x = 1, and y = 0.

2.3.3 Perturbation equations

The base flow is perturbed by a disturbance velocity v and the pressure p' to study the stability of the base flow to disturbances [9].

The total velocity **u** is given by: $\mathbf{u} = U + v$ (8)

and

Pressure $p = P + p'$ (9)

By substituting equations (8) and (9) in equation (4) and (5) respectively, and subtracting equations (6) and (7) we get the equations for the perturbation velocity at no-slip conditions on all boundaries.

The resultant equations obtained are [9]:

$$\nabla . \mathbf{v} = \mathbf{0} \tag{10}$$

$$\mathbf{v}_{,t} + \mathbf{v} \cdot \nabla \mathbf{U} \; + \; \mathbf{U} \cdot \nabla \mathbf{v} \; = -\nabla p' + \frac{1}{Re} \nabla^2 \mathbf{v} \tag{11}$$

The perturbation vorticity transport equation is obtained by taking the curl of equation (11).

$$\boldsymbol{\omega}_{,t} + \nabla \times (\mathbf{U} \times \boldsymbol{\omega}) - \nabla \times (\mathbf{v} \times \boldsymbol{\Omega}) \; = \frac{1}{Re} \nabla^2 \omega \tag{12}$$

where,

ω = perturbation vorticity

Ω = base flow vorticity

In terms of set of potentials ψ and ϕ the velocity (v) and the vorticity(ω) are expressed as follows [9]:

$$\mathbf{v} = \nabla \times (\boldsymbol{i\psi}) + \nabla \times (\mathbf{j}\boldsymbol{\phi}) \tag{13}$$

$$\omega = (\phi_{,xy} - \psi_{,yy} - \psi_{,zz}, \phi_{,zz} - \phi_{,xx} + \psi_{,yx}, \phi_{,xz} + \phi_{,yz}) \tag{14}$$

By expressing equation (12), in terms of these potentials, we get [9]:

$$\mathrm{Re}[\; \omega_{1,t} - (U_1 \omega_2 - U_2 \omega_1)_{,y} - U_1 \omega_{3.z} + \Omega \phi_{,zz}] \; = \nabla^2 \omega_1 \tag{15}$$

$$\mathrm{Re}[\; \omega_{2,t} + (U_1 \omega_2 - U_2 \omega_1)_{,x} - U_2 \omega_{3.z} - \Omega \psi_{,zz}] \; = \nabla^2 \omega_2 \tag{16}$$

The boundary conditions on the potentials are obtained from (13) as:

$\psi_z = \phi_z = 0$ and $\phi_x = \psi_y$

2.4 Stability Analysis:

The above equation can be written as a function of velocity, as follows [2]:

$$\mathbf{u}_{,t} = \mathrm{f}(\mathbf{u}) \tag{17}$$

The flow is further decomposed into a 3D amplitude function and a base flow $\hat{u}$. By considering, the Navier-Stokes equation, a new linearized eigenvalue problem can be represented as follows [2]:

$$\mathbf{u}_{,t} = \frac{\partial \boldsymbol{f}(\bar{\boldsymbol{u}})}{\partial \boldsymbol{u}} \boldsymbol{u}' \equiv \boldsymbol{A}\boldsymbol{u}' \tag{18}$$

where,

A = Jacobian matrix of the RHS of the Navier-stokes equations.

The solution of the eigenmodes of the above equation is [2]:

$$\boldsymbol{u}'(x, y, z, t) = \epsilon \hat{\mathbf{u}}(\boldsymbol{x}, \boldsymbol{y}, \boldsymbol{z}) e^{\lambda \boldsymbol{t}} + \mathbf{c}.\mathbf{c} \tag{19}$$

where,

$\lambda = \lambda_r + i\lambda_i$

where,

λ_i is frequency and λ_r is the amplification and damping rate of the disturbance.

c.c = complex conjugate and

$\epsilon \ll 1$

2.5 Fourier analysis:

Once the perturbations are introduced into the system, to determine the spectral characteristics of the system, the frequency analysis need to be performed. To determine the intensity and frequency response of the system, Fast Fourier Transform (FFT) is used. The discrete signals in time domain are taken by the FFT and transformed into discrete signals in frequency domain. To perform Discrete Fourier Transform (DFT) the Fourier series representation of a signal $f(t)$ is used.

The Fourier transform of time is given by [6]:

$$f(t) = \frac{1}{(2\pi)^{\frac{1}{2}}} \int_{-\infty}^{\infty} f(\omega) e^{-i\omega t}\, d\omega \tag{20}$$

The Fourier transform of frequency is given by [6]:

$$f(\omega) = \frac{1}{(2\pi)^{\frac{1}{2}}} \int_{-\infty}^{\infty} f(t) e^{-i\omega t}\, dt \tag{21}$$

Fourier series for a given periodic function is given by [6]:

$$f(t) = \frac{a_0}{(2\pi)^{\frac{1}{2}}} + \sum_{n=1}^{\infty} (a_n \cos(nt) + b_n \sin(nt)) \tag{22}$$

where the Fourier coefficients a_0, a_n and b_n are given by

$$a_0 = \frac{1}{L}\int_{-L}^{L} f(t)\,dt \tag{23}$$

$$a_n = \frac{1}{L}\int_{-L}^{L} f(t)\cos\left(\frac{n\pi t}{L}\right)dt \qquad n = 1,2,\dots,\infty \tag{24}$$

$$b_n = \frac{1}{L}\int_{-L}^{L} f(t)\sin\left(\frac{n\pi t}{L}\right)dt \qquad n = 1,2,\dots,\infty \tag{25}$$

The discrete signal is then defined as [6]:

$$f(r\Delta t) = f(t)\cdot\delta(t - r\Delta t) \tag{26}$$

where, δ =Dirac delta function defined such that $\delta(0) = 1$ and 0 at all other points.

For, Discrete Fourier transform (DFT) a_n , b_n are replaced by a_k, b_k and given by:

$$a_k = \frac{1}{L}\sum_{r=1}^{2L} f(r\Delta t)\cos\left(\frac{\pi kr}{L}\right) \qquad k = 1,2,\dots,L \tag{27}$$

$$b_k = \frac{1}{L}\sum_{r=1}^{2L} f(r\Delta t)\sin\left(\frac{\pi kr}{L}\right) \qquad k = 1,2,\dots,L-1 \tag{28}$$

The discrete Fourier series $f(r\Delta t)$ for $f(t)$:

$$f(r\Delta t) = \frac{a_0}{2} + \sum_{k=1}^{L-1}\left[\left(a_k\cos\left(\frac{\pi rk}{L}\right) + b_k\sin\left(\frac{\pi rk}{L}\right)\right] + \frac{a_L\cos(\pi r)}{2} \tag{29}$$

3. METHODOLOGY

3.1 OpenFOAM:

OpenFOAM stands for “Open Source Field Operation and Manipulation” [3]. To carry this thesis, OpenFOAM, an open source CFD (Computational Fluid Dynamics) software is used. It is an object-oriented library designed for Computational Continuum Mechanics [5].

OpenFOAM replaces the traditional monolithic software design and user coding extensions by implementing the components of mesh handling, linear system and solver support, discretization operators and physical models in library form [5]. The tools for data acquisition, mesh manipulation and handling, pre-processing etc. are built into this system making its way to the next level of CFD industrial tools [5].

OpenFOAM constitutes of a C++ CFD toolbox which can be used for numerical solvers [3]. These customized numerical solvers can perform a number of simulations which include Multiphase flow, Stress analysis, Turbulence modeling etc. [5].

OpenFOAM implements polyhedral type of mesh handling. In this type of mesh handling, a cell is described as a list of faces closing its volume, a face is an ordered list of point labels and points are gathered into an ordered list of (x, y, z) locations, stored as vectors[5]. The low level implementation is independent of discretization, where the addressing and the mesh metrics such as cell volumes, face areas, cell and face centers etc. is provided by polyMesh class [5]. Basic mesh information is wrapped for convenient use with discretization. fyMesh,

tetFemMesh support the Finite Volume Method (FVM) and the Finite Element (FE) solver respectively[5]. The basic mesh structure and the functionality is shared in both the cases: a single mesh can simultaneously support the FVM and FEM solver without duplication of data and functionality [5]. The OpenFOAM discrete particle modelling solver DPM solver is used in this thesis.

3.2 DPMFoam Solver:

A transient solver that is used for the coupled transport of a single kinematic particle cloud including the effect of the volume fraction of particles on the continuous phase is referred as DPMFoam Solver [5].

3.2.1 Numerical simulation of the gas-solid flow in a fluidized bed by combining DPM with CFD: [2]

Any particle in a fluidized bed experiences two types of motion: Translational ad Rotational [2]. These two motions are completely determined Newton's second law of motion. During its movement, the energy and momentum is exchanged when the particles collide with it's neighboring particles or its walls and interact with the surrounding fluid [2]. The movement of the particles not only is affected by the force originated from the neighbor particles and the surrounding fluid but also gets affected through the disturbance waves produced by far away particles and fluids [2]. To carry out the simulation, a numerical time step less than a critical value is assumed so that disturbance cannot propagate from the particle or the surrounding fluid during single time step [2]. At all times, the resultant force on the particle is determined from its interaction with the neighbor particles and surrounding fluid [2]. Therefore, from all the above

assumptions, according to Newton's second law of motion at a time z, the equation of translational motion of particle i is given by [2]:

$$m_i \frac{dv_i}{d\tau} = f_{f,i} + \sum_{j=1}^{k_i} (f_{c.ij} + f_{d,ij}) + m_i g \quad (30)$$

where,

m_i = mass of particle,

v_i = velocity of particle,

k_i = number of particles in contact with the particle,

$f_{f,i}$= fluid drag force,

$m_i g$= gravitational force,

$f_{c.ij}$= inter-particle forces between particles i and j i.e. contact forces and

$f_{d,ij}$= viscous contact damping force

Since the true density of particle is usually much larger than that of gas, the buoyancy force acting on particle i has been ignored in the above equation [2].

3.2.2. Inter-particle forces:

The torque T_{ij} is generated due to internal-particle forces acting at the contact point between particles i and j, causing particle i to rotate. For a spherical radius R_i, the torque T_{ij} is given by [2]:

$$T_{ij} = R_i * f_{c,ij} \quad (31)$$

Therefore, the rotational motion of particle i is given by [2]:

$$I_i \frac{d\omega_i}{d\tau} = \sum_{j=1}^{k_i} T_{ij} \quad (32)$$

where,

ω_i= angular velocity,

I_i= moment of inertia of particle $i = \frac{2}{5} m_i R_i^2$

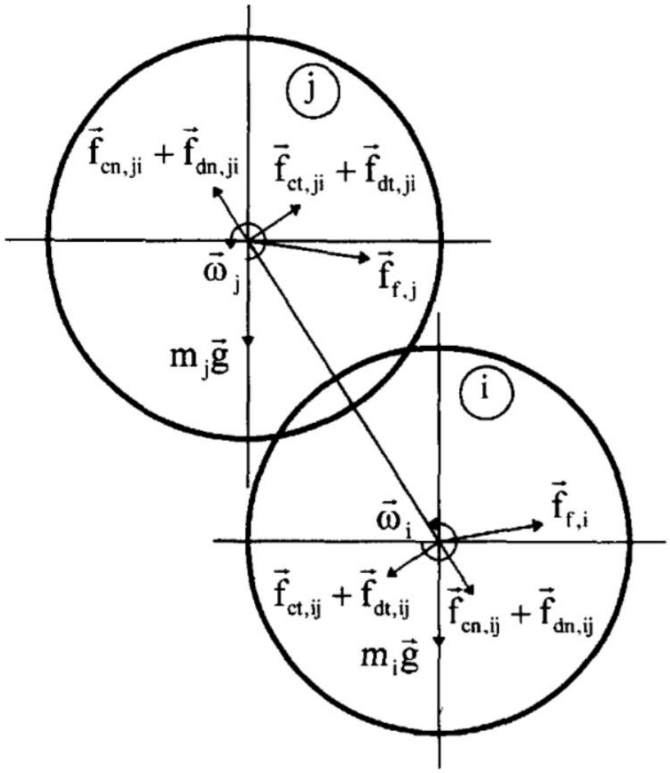

Figure 3.1 Schematic illustration of the forces acting on colliding particles *i* and *j* [2]

The linear normal and tangential contact force models exhibited by the particles are given by [2]:

$$f_{cn,ij} = -(k_{n,i}\delta_{n,ij})n_i \quad (33)$$

and

$$f_{ct,ij} = -(k_{t,i}\delta_{t,ij})t_i \quad (34)$$

where,

$k_{n,i}$, = spring constant in normal direction

$\delta_{n,ij}$= displacement between particles i and j in normal direction

$k_{t,i}$, = spring constant in tangential direction

$\delta_{t,ij}$= displacement between particles i and j in tangential direction

n_i= the unit vector along the normal direction for particle i

t_i= the unit vector along the tangential direction for particle i

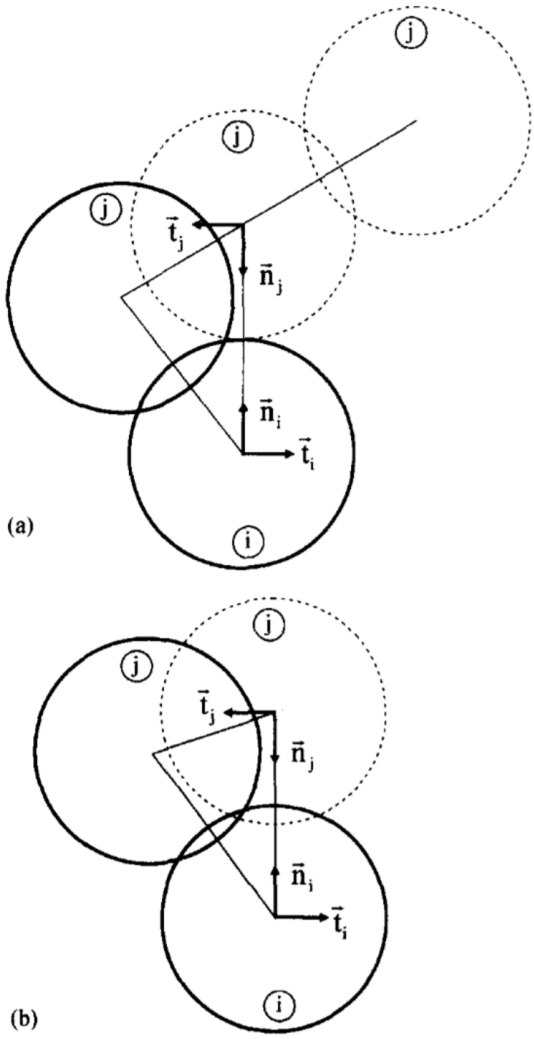

Figure 3.2 Relative positions between particles *i* and *j* before collision: (a) separated; (b) contacted [2]

The magnitude of the tangential force is given by Coulomb law [2]:

$$|f_{ct,ij}| = -\gamma_{ij}|f_{cn,ij}|, \tag{35}$$

where, γ_{ij} = the coefficient of friction between particles i and j

As a result of inelastic collisions, when no external energy is added; the system tends to be stationary and can be simulated by introducing a viscous contact damping force to consume the system energy during the particle collisions [2].

For a particle i, the viscous contact damping forces along the normal and tangential directions are, respectively, given by [2]:

$$f_{dn,ij} = -\eta_{n,i}(v_r . n_i)n_i \tag{36}$$

$$f_{dt,ij} = -\eta_{t,i}[(v_r . t_i)t_i + (\omega_i \times R_i - \omega_j \times R_j)] \tag{37}$$

where,

$f_{dn,ij}$ = viscous contact damping forces for particle i along the normal direction

$f_{dt,ij}$= viscous contact damping forces for particle i along the tangential direction

$\eta_{n,i}$ = viscous contact damping coefficient for particle i along the normal direction

$\eta_{t,i}$ = viscous contact damping coefficient for particle i along the tangential direction

v_r= velocity vector of particle i relative to $j = v_i - v_j$

3.2.3 Drag Force:

Fluid drag force is dependent on relative velocity of fluid and particle surroundings. According to Di Felice (1994), the fluid drag force acting on a single particle applicable to fluidized and fixed beds over the full practical range of particle Reynolds number is given by [2]

$$f_{f,i} = f_{f0,i}\varepsilon_i^{-x} \tag{38}$$

where,

ε_i= porosity in a computational cell in which particle i is located

$f_{f0,i}$ = fluid drag fore on particle i in the absence of other particles

$$= 0.5\, c_{d0,i}\rho_f \pi R_i^2 |u_i - v_i|(u_i - v_i) \quad (39)$$

Fluid drag coefficient $c_{d0,i} = (0.63 + \frac{4.8}{Re_{\rho,i}^{0.5}})^2$ (40)

Reynolds number $Re_{\rho,i} = \frac{2\rho_f R_i |u_i - v_i|}{\mu_f}$ (41)

ρ_f= fluid density and μ_f= viscosity

x = empirical coefficient = $3.7 - 0.65 \exp[-\frac{(1.5 - \log_{10} Re_{\rho,i})^2}{2}]$ (42)

3.3 Particle-fluid Coupling:

The Fluid-Particle Coupling is a 4 way approach. The new version of OpenFOAM includes particle drag models that are suitable for dense particle flows [4]:

- **WenYu**: suitable for particulate volume fractions up to approximately 0.2.
- **ErgunWenYu**: suitable for all particulate volume fractions up to the closed packed condition.
- **PlessisMasliyah**: suitable for all particulate volume fractions up to the closed packed condition.

Ergun-Wen-Yu drag model for solid spheres pressure drop is given by [11]:

For Ergun, Pressure drop $K_{sg} = 150 \frac{\mu_g \alpha_s^2}{d_p^2 \alpha_g^2} + 1.75 \frac{\rho_g \alpha_s}{d_p \alpha_g} |\mathbf{u}_g - \mathbf{u}_s|$ (43)

For Wen-Yu, Pressure drop $K_{sg} = 0.75 \frac{C_d \alpha_s \alpha_g^{-1.65} \rho_g}{d_p} \left| \mathbf{u}_g - \mathbf{u}_s \right|$ (44)

3.4 Slip Velocity:

Slip velocity in two-phase (solid-liquid) flow, is defined as the ratio of the velocity of the gas phase to the velocity of the liquid phase. In the homogeneous model of two-phase flow, the slip ratio is by definition assumed to be unity (no slip) [12]

$$v_{sl} = \frac{d_s^2 g(\rho_s - \rho_f)}{18\mu} \quad (45)$$

where

μ = Newtonian viscosity of the fluid, in Pa-s = $1.983 * 10^{-5}$ Pa-s

d_s = particle diameter, m = 0.0025 m

v_{sl} = particle slip velocity, m/s

ρ_s = solid density, kg/m^3 = 0.6,1.2 and 2.4

ρ_f = fluid density, kg/m^3 = 1.2

g = acceleration of gravity, m/s^2 = 9.81

3.5 Collision Dynamics:

In a gas fluidizes bed, the fast moving particles exhibit complicated collision patterns [2]. The collision partners, including the collision points change during the time evolution. During this time, there is a high possibility for a particle to collide with its collision partner via free fly path. Free fly path, when not considered properly introduces a fictitious elastic energy that is

stored in the particles. This problem is can be explained using a two-dimensional collision dynamic model [2].

Consider a movement of particle j relative to i within a time step $\Delta\tau$. At the current time, the two particles will be in contact. At the previous time, two possibilities exist: the two particles are either contacted or separated. If the two particles are separated before the collision, the position at which j touches i is found by moving particle j in backward direction along the direction of their relative velocity to a point at which the distance between the mass centers is equal to sum of the radii [2]. The actual collision time from this point is given by $\Delta\tau^1$ and is less than $\Delta\tau$ [2].

$$\Delta\tau^1 = -\frac{(av_x+bv_y)+\sqrt{(av_x+bv_y)^2+v_r^2(R^2-L^2)}}{v_r^2} \tag{46}$$

If (x_i, y_i) and (x_j, y_j) are the Cartesian coordinates of the particles i and j, v_x and v_y are the relative velocities in x and y direction respectively [2];

$$a = x_j - x_i \tag{47}$$

$$b = y_j - y_i \tag{48}$$

$$R = R_i + R_j \tag{49}$$

$$L = \sqrt{a^2 + b^2} \tag{50}$$

$$v_r = |v_i - v_j| \tag{51}$$

During time step $\Delta\tau^1$, the incremental displacements in normal and tangential direction respectively, are given by [2]:

$$\Delta\delta_{n,i,j} = (v_r . n_i)\Delta\tau^1 \quad (52)$$

and

$$\Delta\delta_{t,i,j} = (v_r . t_i + \left(\omega_i * R_i - \omega_j * R_j\right). t_i)\Delta\tau^1 \quad (53)$$

During time step $\Delta\tau$, the incremental displacements in normal and tangential direction respectively, are given by [2]:

$$\Delta\delta_{n,i,j} = (v_r . n_i)\Delta\tau \quad (54)$$

and

$$\Delta\delta_{t,i,j} = (v_r . t_i + \left(\omega_i * R_i - \omega_j * R_j\right). t_i)\Delta\tau \quad (55)$$

3.6 Computational Fluid Dynamics:

The particles in the gas fluidized bed create impermeable boundaries which force the gas to flow through the interstitial gaps by detouring from the path. A fluid drag force is produced by the gas flow which with the inter-particle forces results in the motion of individual particles [2]. Through this mutual interaction, the energy and the momentum are exchanged between the continuum gas and discrete particles. And this interaction complicates the flow pattern in the fluidized bed so that the point variables of gas phase vary rapidly in both space and time [2]. To calculate these instantaneous point variables of gas phase with moving discrete boundaries and a number of particles, the mass conservation and Navier-Stokes equation are used [2].

$$\frac{\partial\varepsilon}{\partial\tau} + \nabla.(\varepsilon u) = 0 \quad (56)$$

and

$$\frac{\partial(\rho_f \varepsilon u)}{\partial \tau} + \nabla.\left(\rho_f \varepsilon \mathrm{uu}\right) = -\varepsilon \nabla \rho - F + \nabla.(\varepsilon \Gamma) + \rho_f \varepsilon \mathrm{g} \tag{57}$$

where,

ρ = fluid pressure,

F = volumetric fluid-particle interaction force = $\frac{\Sigma_{i=1}^{k_c} \mathrm{f}_{f,i}}{\Delta V}$ (58)

where,

ΔV= volume of the computational cell = $\Delta x \Delta y \Delta z$

$\Delta x, \Delta y, \Delta z$ = lengths of a computational cell in x, y and z direction respectively

k_c= number of particles located in the cell

ε = porosity = $1 - \frac{\Sigma_{i=1}^{k_c} V_i}{\Delta V}$ (59)

where,

V_i= volume of particles i inside a computational cell

Γ = viscous stress tensor

⇨ $\Gamma = \left[\left(\mu_f' - \frac{2}{3}\mu_f\right)\nabla.\mathrm{u}\right]\delta_k + \mu_f[(\nabla \mathrm{u}) + (\nabla \mathrm{u})^{-1}$ (60)

where,

δ_x = Kronecker delta and

μ_f' = fluid bulk viscosity

3.7 Solution technique:

Different governing equations and different solution schemes have be used in the Discrete Particle Method (DPM) and Computational Fluid Dynamics (CFD). To solve the translational and rotational motions in the DPM simulations, the explicit time integration method is used. The main advantage of this method is the straight forward formulation, but to the numerical stability constraints, the time step used must be small for this simulation because until the particles finish the movement in one time step, they do not detect the contact with others. During this process, the displacements might me overestimated sometimes, which results in the fictitious elastic energy for the particle collisions. The predictor-corrector method is introduced to the present simulation in order to avoid this problem [2].

The following equations are uses in the predictor-corrector procedure.

Predictor stage [2]:

$$v_i^p = v_i + \Delta\tau(1-\alpha)a_i \tag{61}$$

$$r_i^p = r_i + \Delta\tau v_i + 0.5\Delta\tau^2(1-2\beta)a_i \tag{62}$$

The force balance after predictor stage is [2]:

$$m_i a_i^p = \mathrm{f}_{f.i} + \sum_{j=1}^{k_c}\left(\mathrm{f}_{c,i,j}^p + \mathrm{f}_{d,i,j}^p\right) + m_i g \tag{63}$$

Corrector stage [22]:

$$v_i^c = v_i^p + \Delta\tau\alpha a_i^p \tag{64}$$

$$r_i^c = r_i^p + \Delta\tau^2\beta a_i^p \tag{65}$$

where,

a_i, r_i = acceleration and position vector of particle i, respectively,

superscripts p, c = values estimated at the predictor and corrector stages,

α, β = the Newmark parameters which control the accuracy and stability of the method

To solve the CFD equations, the conventional SIMPLE method is used. The basic governing equations are discretized in finite volume form on a uniform, staggered grid. For the pressure gradient and divergence terms second-order central difference scheme is used. To solve the convection term the first order up-wind scheme is used while for the time derivative a second-order Crank-Nicolson scheme is used [2].

3.8 GAEA NIU [13]:

For any CFD analysis, the factors that need to be considered are: the accuracy, computational time, model and geometry. The solver time for the analysis depends on the number of dimensions, mesh and the geometry. Apart from these another important factor is the computer specifications. The factors such as the memory, processor specifications, random access memory (RAM) size and graphics affect the analysis time. However, to save the time, scaling and parallel computing can be used which also increases the efficiency and reliability.

For this analysis Gaea NIU- super computer is used Gaea is a 60-node CPU/GPU hybrid cluster. Each node is an HP SL380s G7 equipped with 72 GB RAM, 2 Intel X5650 2.66 GHz 6-core processors, four 500 GB 2.5” SATA disk drives and 2 NVIDIA M2070 FERMI GPUs, each with 6GB RAM and connected via PCI-E. All 60 nodes are connected via Full 1:1 non-blocking Infiniband and Ethernet switch connectors[13].

The cluster also has two storage servers, each an HP Proliant DL380G7 server, and an HP P2000 disk storage array with 192 TB of effective storage space (i.e., after RAID6) [13]. The storage array is connected to the storage servers via 6 Gigabit per second SAS connections [13].

4. RESULTS AND DISCUSSION

4.1 Benchmark

4.1.1 Ghia, et al. *High-Re Solutions for Incompressible Flow Using N-S Equations – 1982*

The first step of this thesis is to validate the system and the approach. To do this, the work was done on the square cavity that is the generic lid driven cavity with single phase and the results are compared to Ghia et al [10]. This paper represents the benchmark for 2D analysis and this is an effort to employ the multigrid method in the solution of the stream function-vorticity equations for a model flow problem with a goal of obtaining solutions for Reynolds numbers and mesh refinements as high as possible [10].

The grid size of 129 x 129 up to 257 x 257 is used in this paper, to acquire the results for the Reynolds number ranging between 100-10,000 [10]. The analysis was carried out without particles to approach steady-state in the lid-driven cavity. These results are used as benchmark for relative horizontal velocity along the centerline for Reynolds numbers 100,400 and 1000. The convergence criteria for this analysis is set as 10^{-6} and the simulation time is 10 seconds [10].

The present results are compared to Ghia, and shown below in the figures 4.1, 4.3 and 4.3 for various Reynolds numbers.

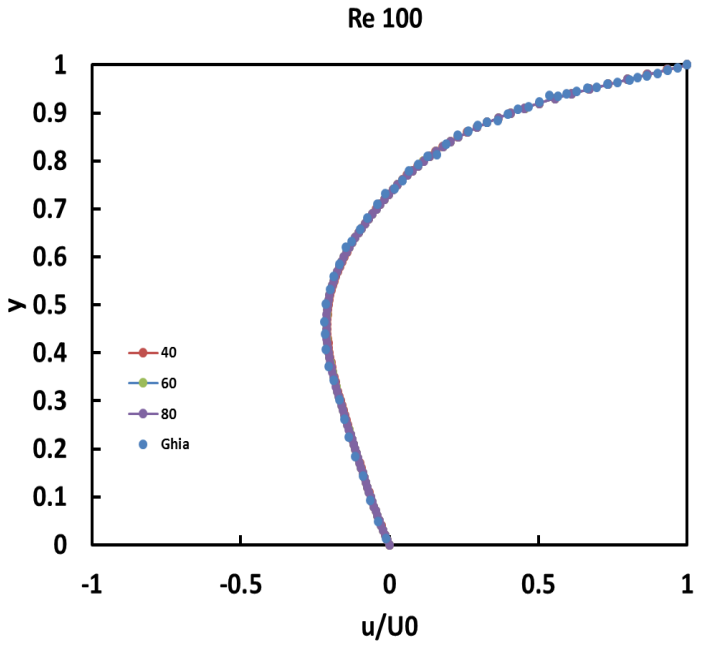

Figure 4.1 Re100 2D centerline velocities

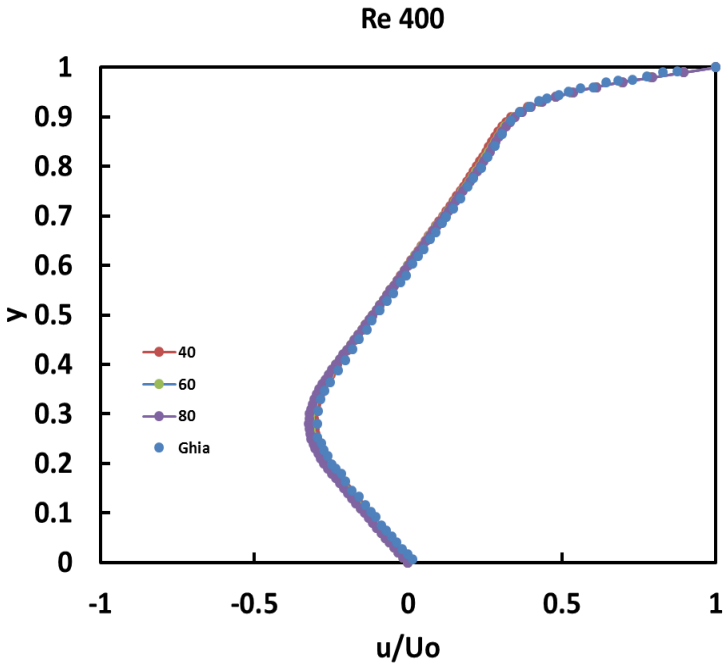

Figure 4.2 Re400 2D centerline velocities

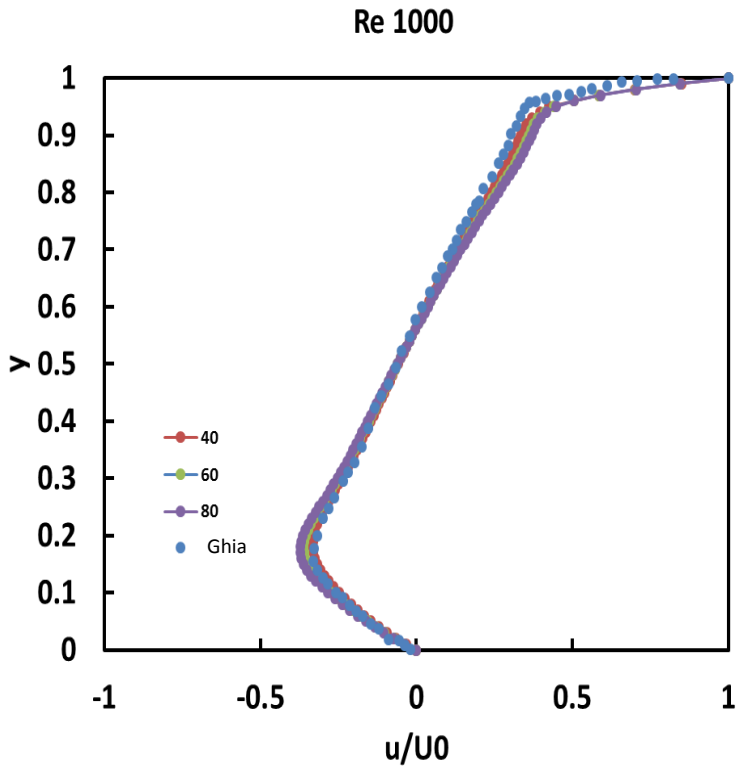

Figure 4.3 Re1000 2D centerline velocities

From the above results, it is observed that for the Reynolds number 100, the solver provided accurate results with less number of grids which indicates that a fine grid is not necessary for low Reynolds number. As the grid size increases to 80, the percent difference with Ghia's results greatly reduces.

The error percentage with respect to Ghia is shown is given by the formula below:

$$\%Error = \frac{U_{Ghia} - U_{current}}{U_{Ghia}}$$

The error percentage for Centerline Velocity Comparison, for the Reynolds number 100,400 and 1000 compared to Ghia and shown below in the figure 4.4, 4.5 and 4.6.

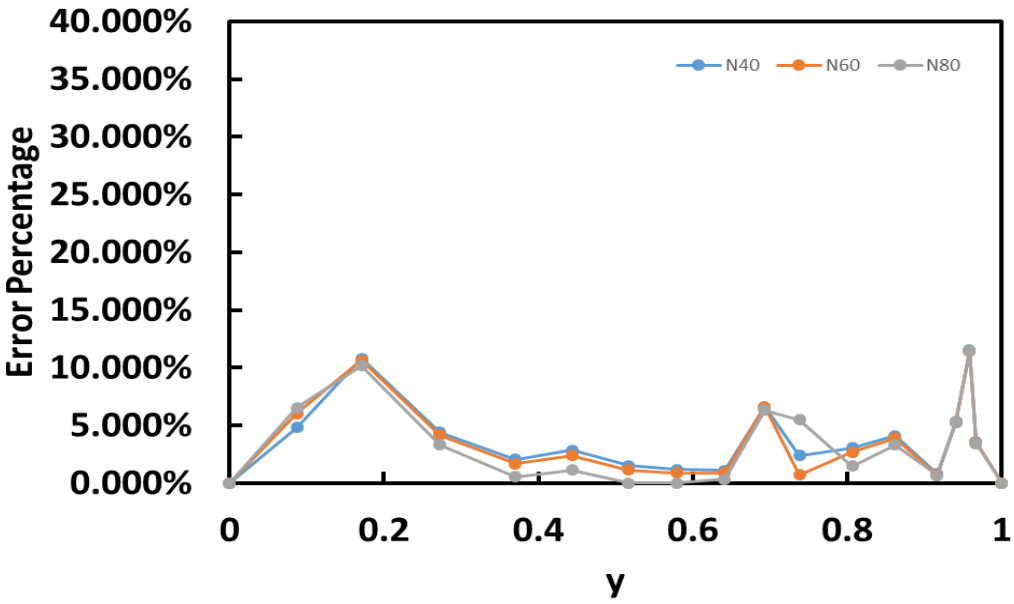

Figure 4.4 Error Analysis of Re100 2D centerline velocities

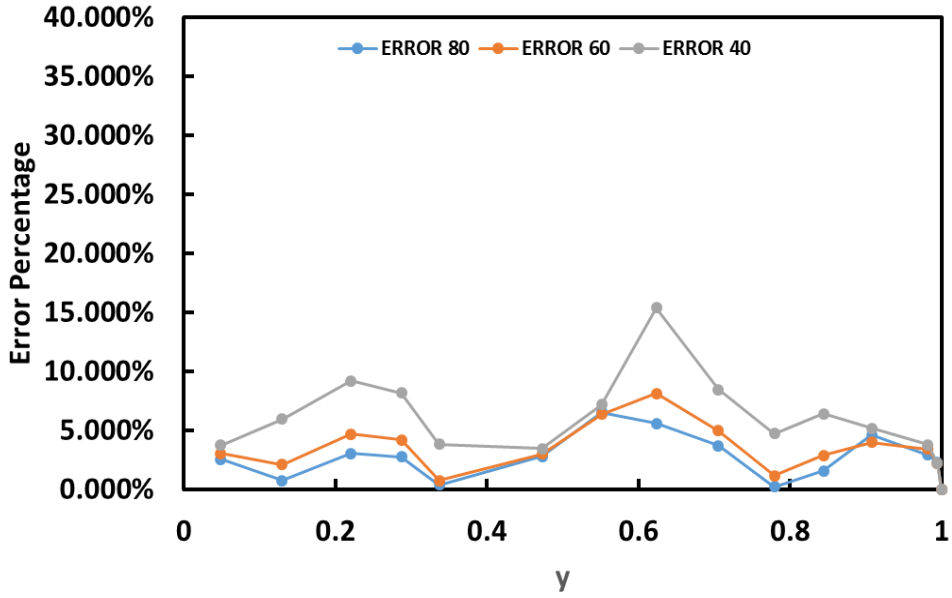

Figure 4.5 Error Analysis of Re400 2D centerline velocities

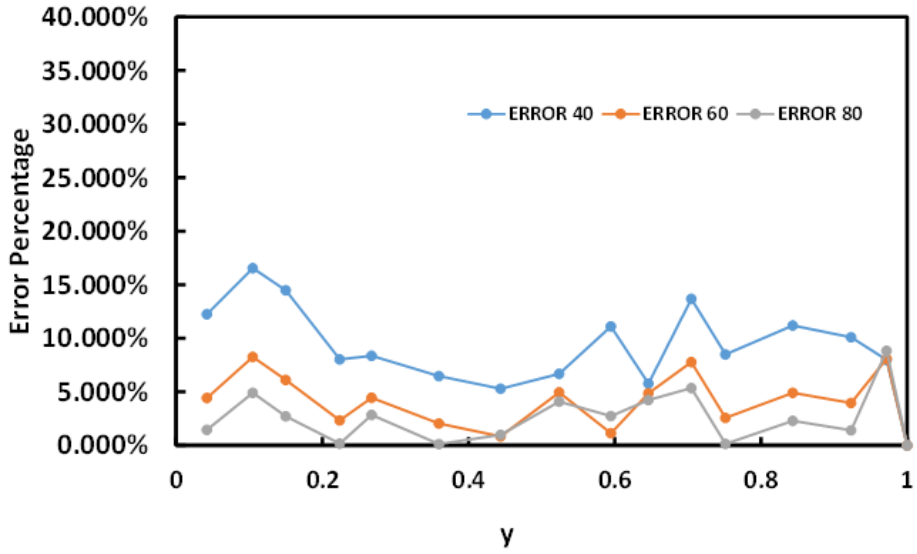

Figure 4.6 Error Analysis of Re1000 2D centerline velocities

4.1.2 Kumar, et al. Mathematical and simulation of lid driven cavity flow at different aspect ratios using single relaxation time lattice boltzmann technique – 2013

In this paper Single Relaxation Time (SRT) Lattice Boltzmann equation have been used to simulate 2D lid driven cavity flow at various Reynolds numbers and three aspect ratios, K=1, 1.5 and 4 [1]. These results are used as benchmark for relative horizontal velocity along the centerline for K= 1.5 and Reynolds numbers 100,400 and 1000 with the boundary conditions imposed in this paper is no-slip and constant inlet velocity [1].

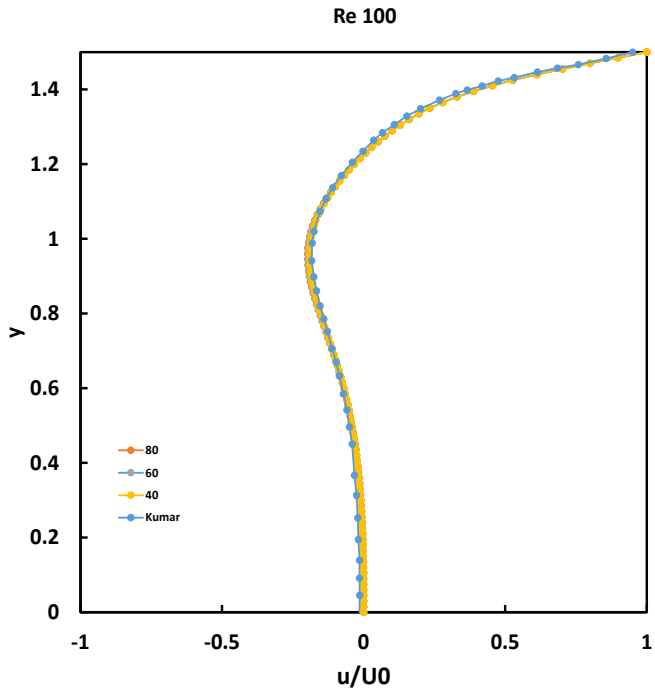

Figure 4.7 Re100 2D centerline velocities for K= 1.5

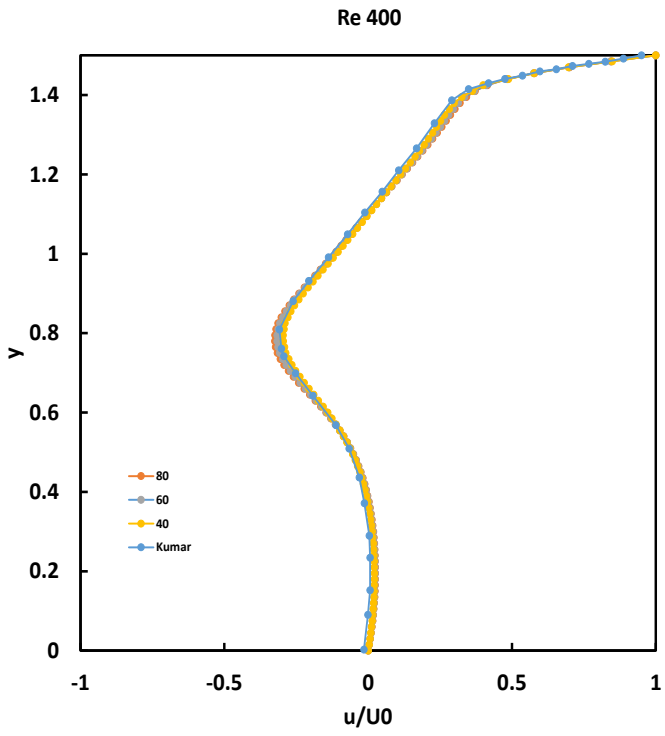

Figure 4.8 Re400 2D centerline velocities for K= 1.5

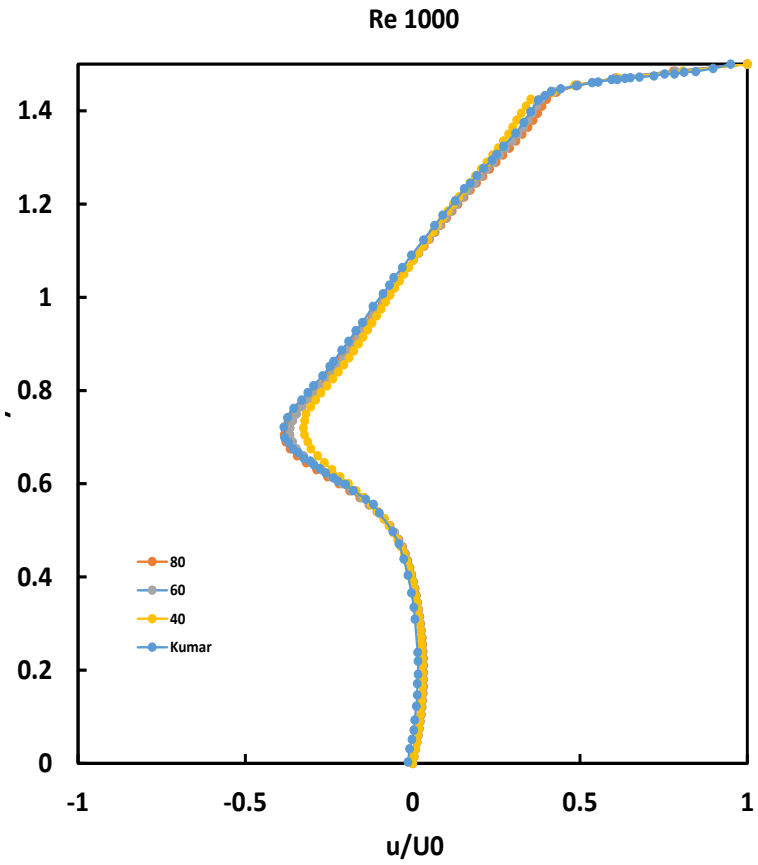

Figure 4.9 Re1000 2D centerline velocities for K= 1.5

The error percentage is calculated for Reynolds number 100,400 and 1000 and is shown below. From the error analysis graphs it can be stated that maximum error of 28% is seen when Reynolds number is 1000.

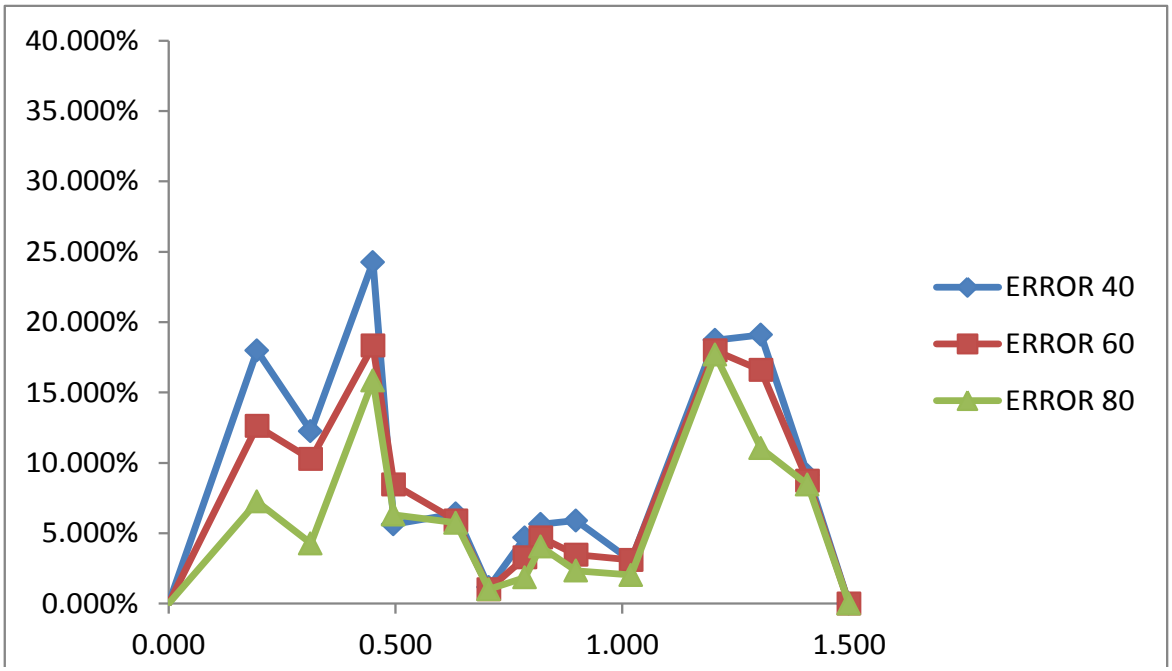

Figure 4.10 Error Analysis of Re100 2D centerline velocities for K=1.5

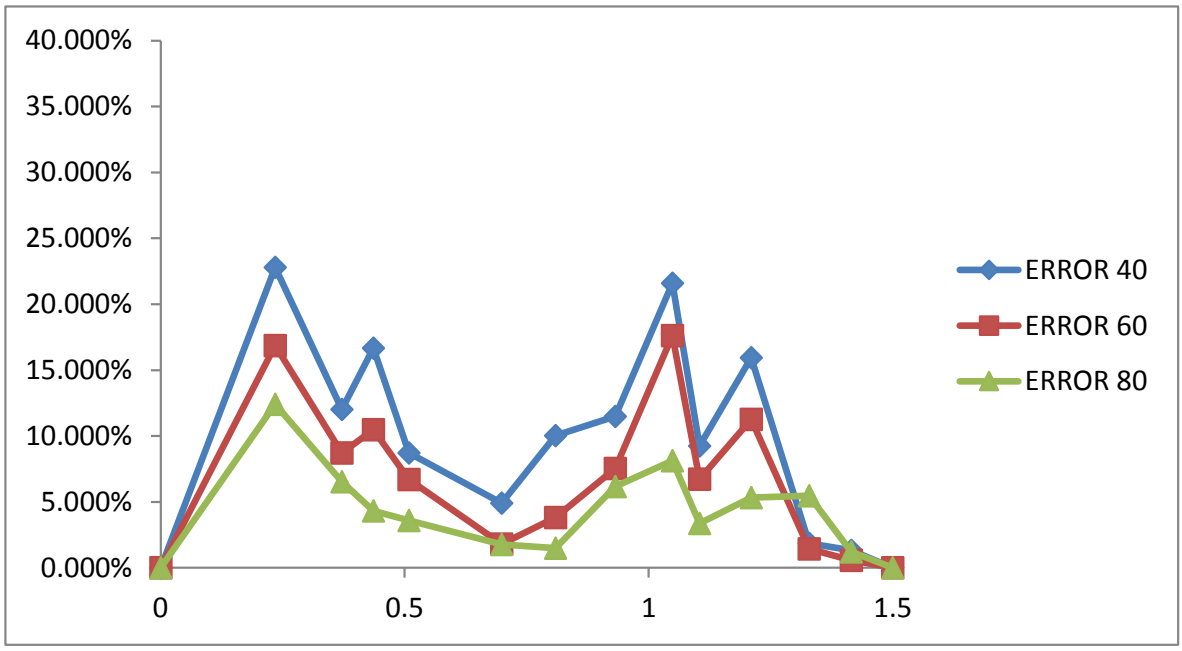

Figure 4.11 Error Analysis of Re400 2D centerline velocities for K=1.5

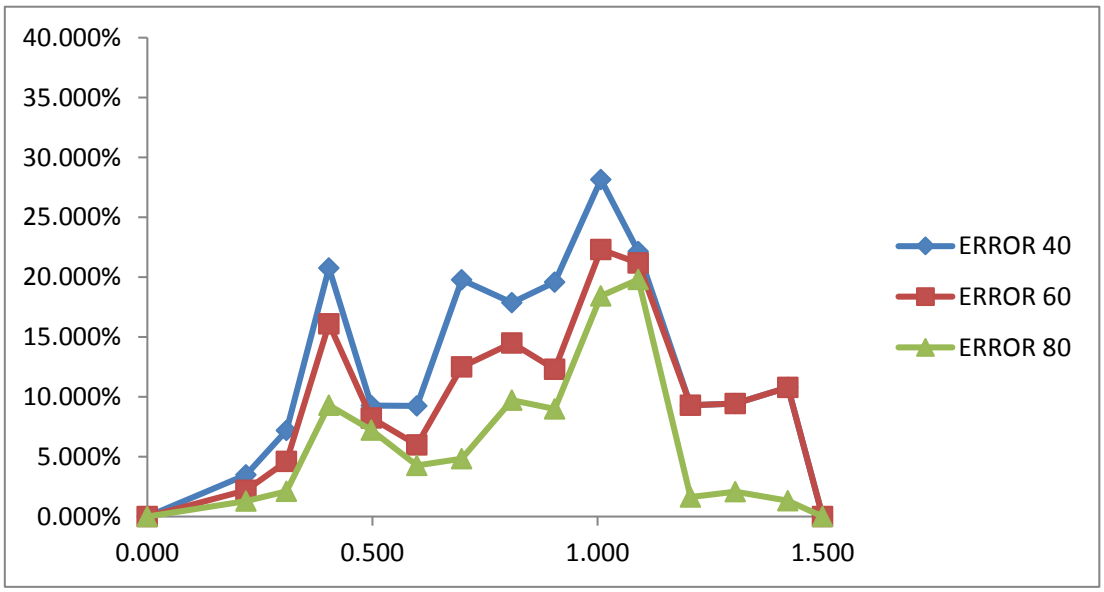

Figure 4.12 Error Analysis of Re1000 2D centerline velocities for K=1.5

4.2 Cases Calculated

In this thesis three independent variables namely, the Reynolds number, particle concentration and particle density were evaluated. A particle concentration of 25, 50 or 75 percent was suspended into the fluid at the Reynolds numbers 100, 400 and 1000 respectively, at the density ranged from half, double and equal to the density of the working fluid, as shown in the Table 1 below:

Table 1: Cases

$\rho_1 = \frac{\rho_p}{\rho_f} = 0.5$			
ϕ_1 = 25 %	Re100	Re400	Re1000
ϕ_2 = 50 %	Re100	Re400	Re1000
ϕ_3 = 75 %	Re100	Re400	Re1000
$\rho_2 = \frac{\rho_p}{\rho_f} = 1$			
ϕ_1 = 25 %	Re100	Re400	Re1000
ϕ_2 = 50 %	Re100	Re400	Re1000
ϕ_3 = 75 %	Re100	Re400	Re1000
$\rho_3 = \frac{\rho_p}{\rho_f} = 2$			
ϕ_1 = 25 %	Re100	Re400	Re1000
ϕ_2 = 50 %	Re100	Re400	Re1000
ϕ_3 = 75 %	Re100	Re400	Re1000

4.3 Particle Description

The particles are initially placed in the middle of the cavity along the horizontal at the beginning of the simulation. As the density concentration increases, the particles are expanded along the vertical direction. The particles are placed at a distance of 2.5mm from each other at the start of the simulations.

4.4 Settling Time

Through the depth of lid-driven cavity 10 points are selected on the centerline of the cavity dividing it into equal parts Y= 0.1 to Y = 1 and then velocities at these points in the direction of the velocity of the moving lid of the lid-driven cavity are plotted over time. These plots are referred as Settling Time plots below.

The transient flow characteristics can be observed in the figures below. For the figures 4.13, 4.14 and 4.15 a very low drag can be observed and the Ux is never negligible and amplitude of oscillations of Ux decreases gradually reaching the steady state.

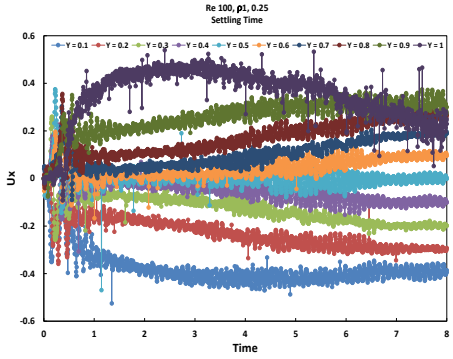

Figure 4.13 Re 100, ρ_1, ϕ = 0.25 velocity over time

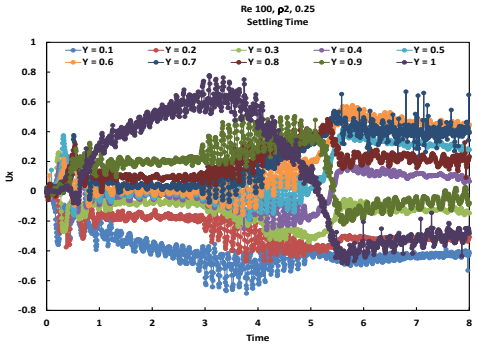

Figure 4.14 Re 100, ρ_2, ϕ = 0.25 velocity over time

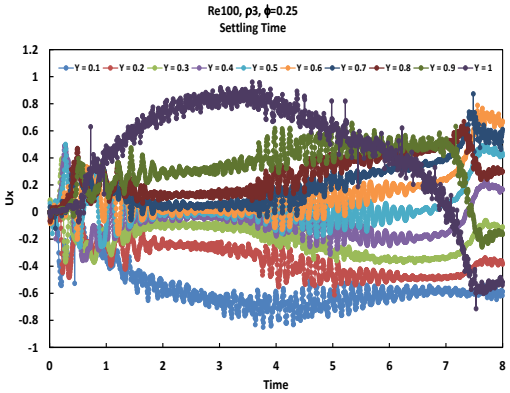

Figure 4.15 Re 100, ρ_3, ϕ = 0.25 velocity over time

Low drag is observed in the figures 4.16 to 4.21, 4.25 to 4.30 and 4.43 to 4.39 below. Also, Ux is negligible until only 1.5 seconds and increases suddenly; and takes very less time to reach steady state.

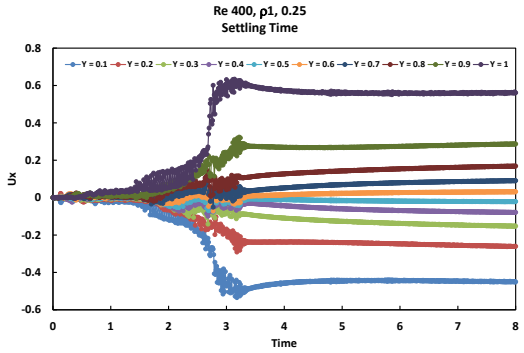

Figure 4.16 Re 400, ρ_1, ϕ = 0.25 velocity over time

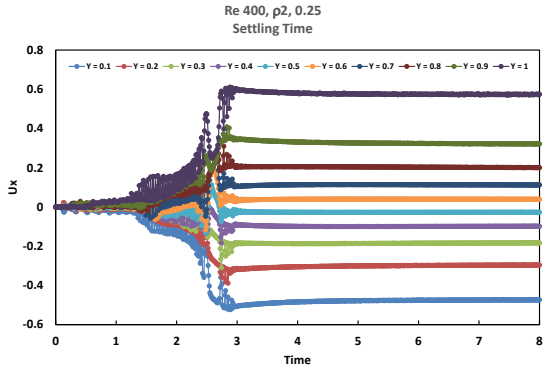

Figure 4.17 Re 400, ρ_2, ϕ = 0.25 velocity over time

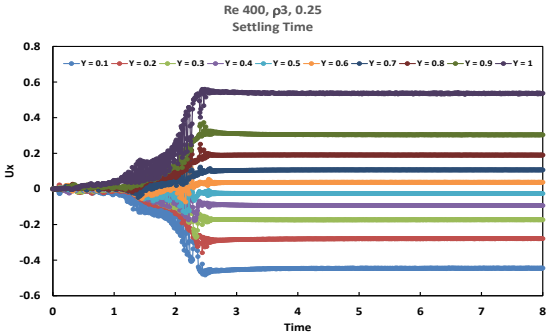

Figure 4.18 Re 400, ρ_3, ϕ = 0.25 velocity over time

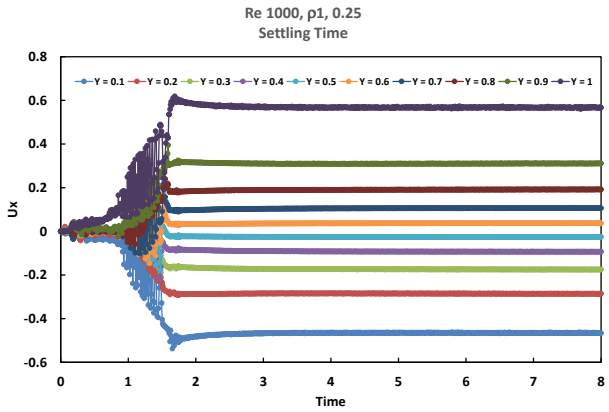

Figure 4.19 Re 1000, ρ_1, ϕ = 0.25 velocity over time

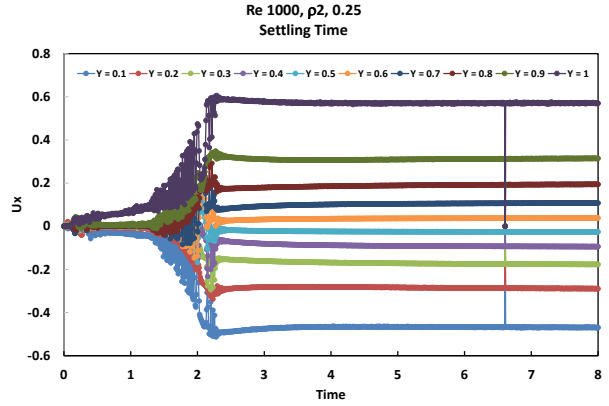

Figure 4.20 Re 1000, ρ_2, ϕ = 0.25 velocity over time

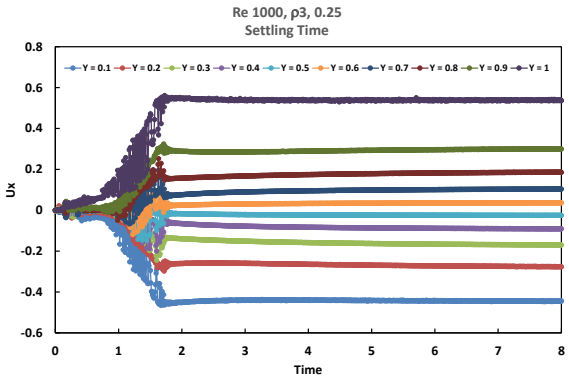

Figure 4.21 Re 1000, ρ_3, ϕ = 0.25 velocity over time

High drag is observed in the figures 4.22 to 4.24 and 4.31 to 4.33 below. Also, Ux is negligible till 2.5 seconds and increases gradually in the form of smooth curves until it reaches steady state

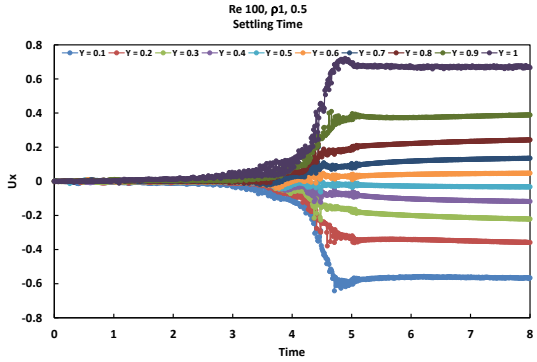

Figure 4.22 Re 100, ρ_1, ϕ = 0.5 velocity over time

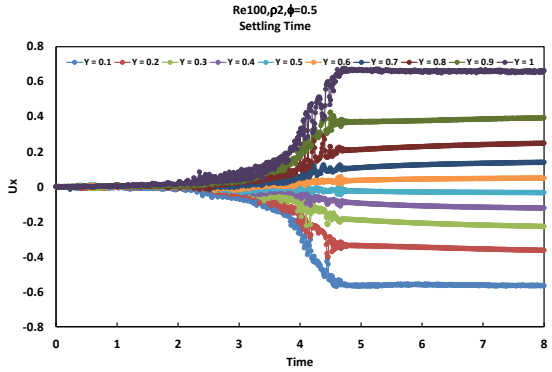

Figure 4.23 Re 100, ρ_2, ϕ = 0.5 velocity over time

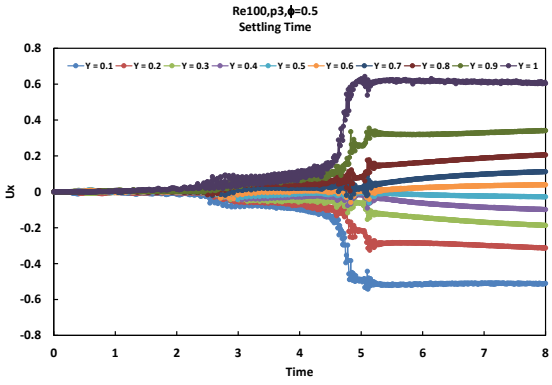

Figure 4.24 Re 100, ρ_3, ϕ = 0.5 velocity over time

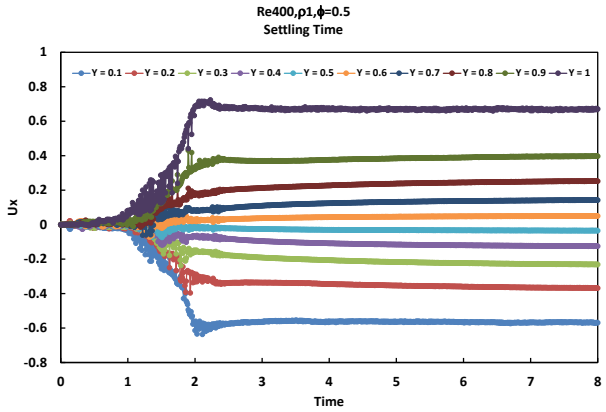

Figure 4.25 Re 400, ρ_1, ϕ = 0.5 velocity over time

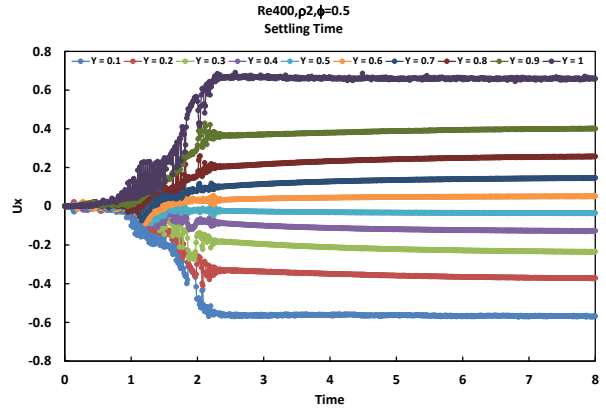

Figure 4.26 Re 400, ρ_2, ϕ = 0.5 velocity over time

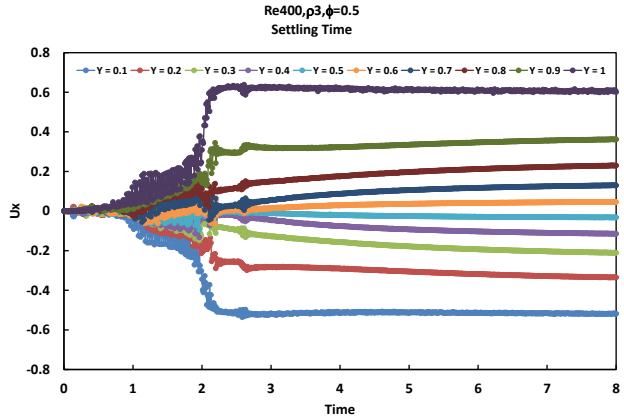

Figure 4.27 Re 400, ρ_3, ϕ = 0.5 velocity over time

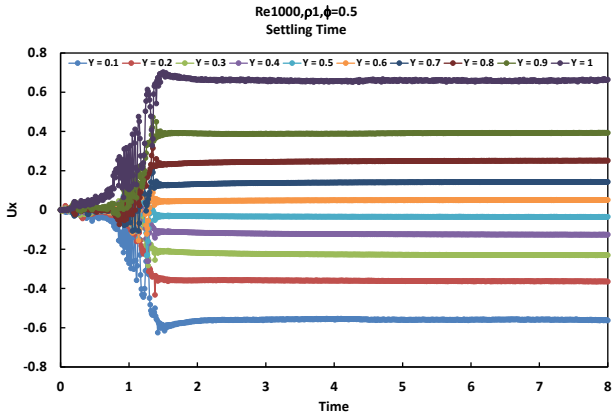

Figure 4.28 Re 1000, ρ_1, ϕ = 0.5 velocity over time

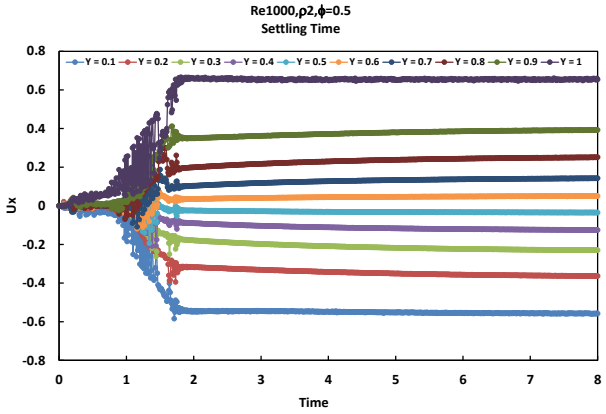

Figure 4.29 Re 1000, ρ_2, ϕ = 0.5 velocity over time

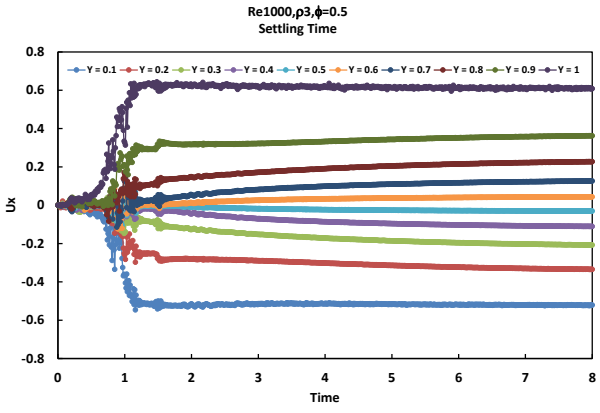

Figure 4.30 Re 1000, ρ_3, ϕ = 0.5 velocity over time

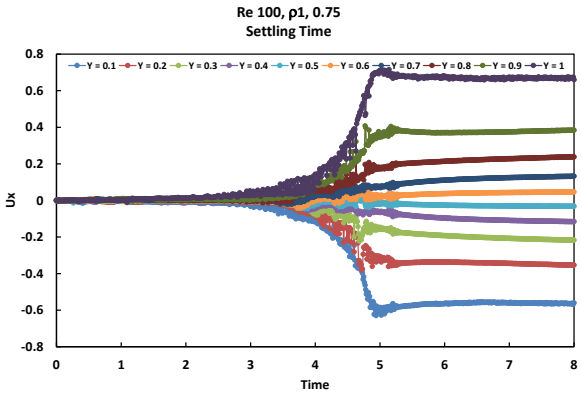

Figure 4.31 Re 100, ρ_1, ϕ = 0.75 velocity over time

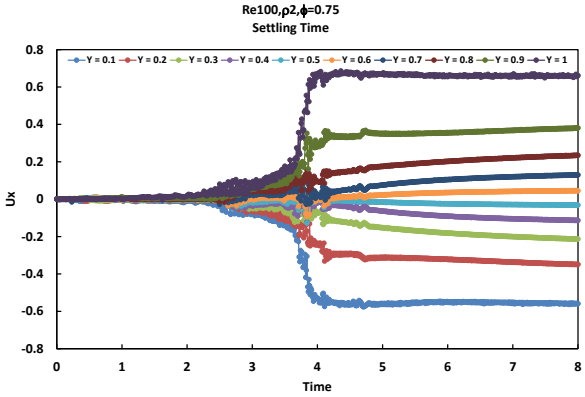

Figure 4.32 Re 100, ρ_2, ϕ = 0.75 velocity over time

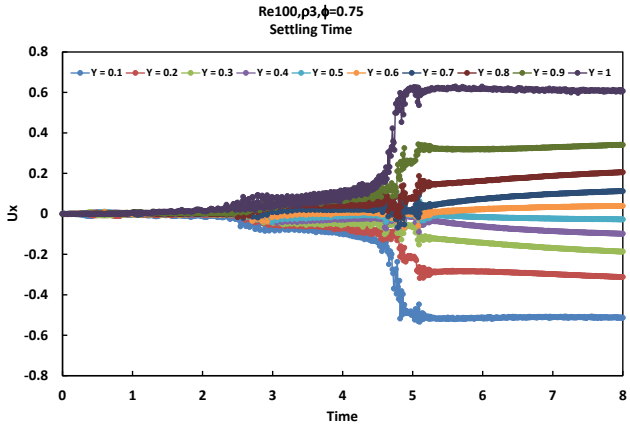

Figure 4.33 Re 100, ρ_3, ϕ = 0.75 velocity over time

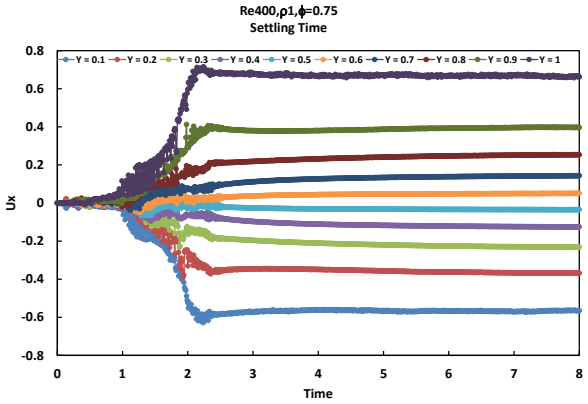

Figure 4.34 Re 400, ρ_1, ϕ = 0.75 velocity over time

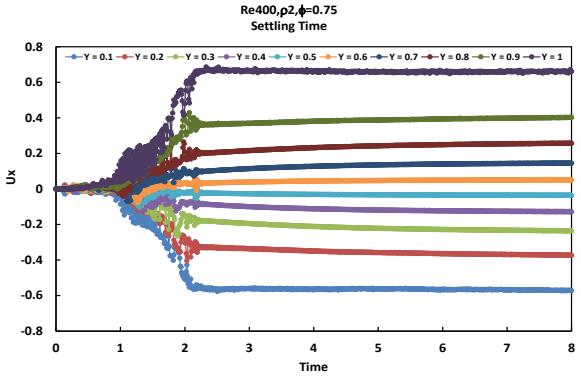

Figure 4.35 Re 400, ρ_2, ϕ = 0.75 velocity over time

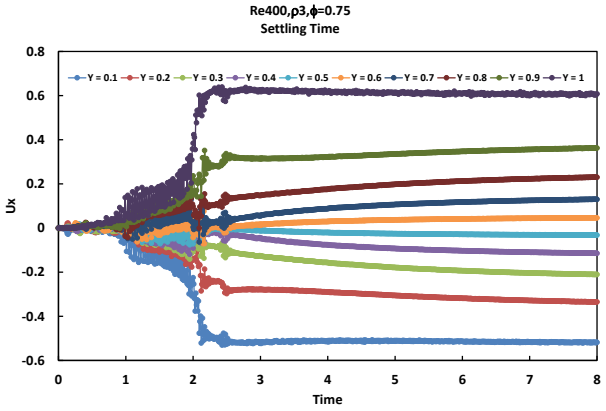

Figure 4.36 Re 400, ρ_3, ϕ = 0.75 velocity over time

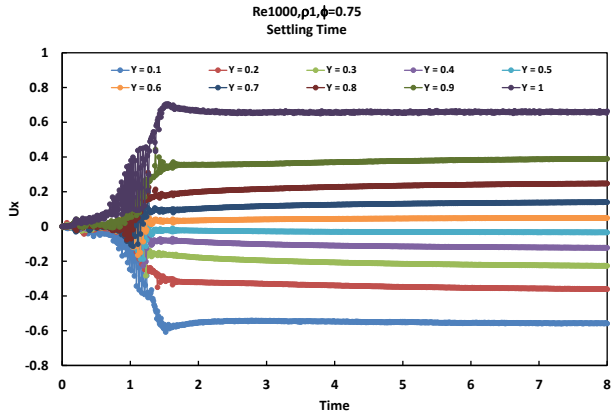

Figure 4.37 Re 1000, ρ_1, ϕ = 0.75 velocity over time

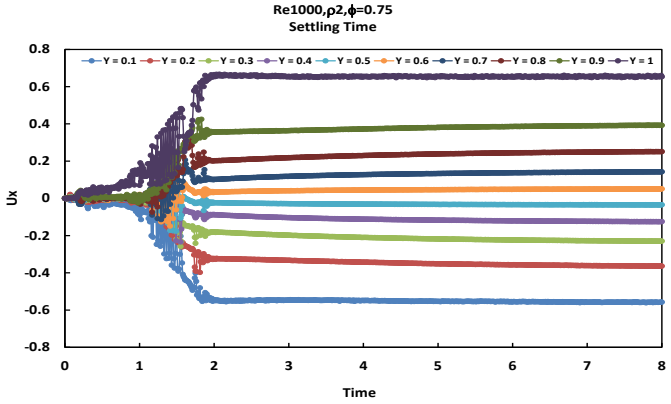

Figure 4.38 Re 1000, ρ_2, ϕ = 0.75 velocity over time

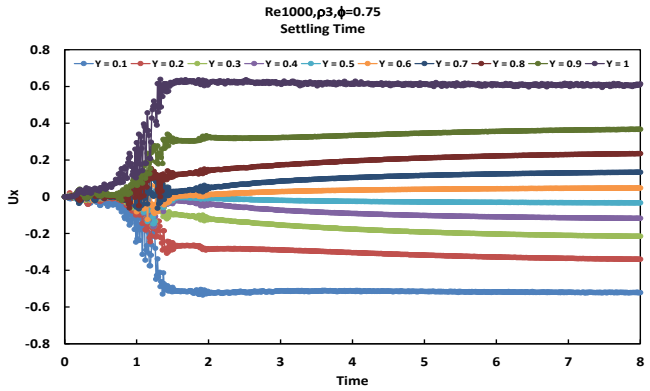

Figure 4.39 Re 1000, ρ_3, ϕ = 0.75 velocity over time

4.5 Spectral Analysis

In this section, by means of Fourier transform the frequency component of the velocity is examined. Through the depth of lid-driven cavity 10 points are selected on the centerline of the cavity dividing it into equal parts Y= 0.1 to Y = 1 and then frequency analysis was performed at these points. The settling time data is used to perform the frequency analysis.

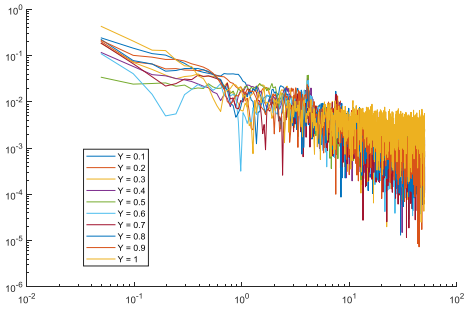

Figure 4.40 Re 100, ρ_1, ϕ = 0.25

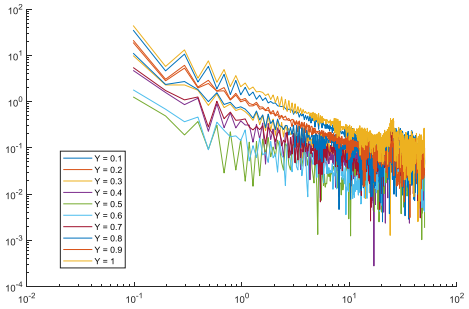

Figure 4.41 Re 400, ρ_1, ϕ = 0.25

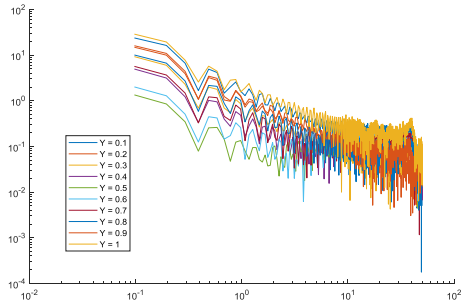

Figure 4.42 Re 1000, ρ_1, ϕ = 0.25

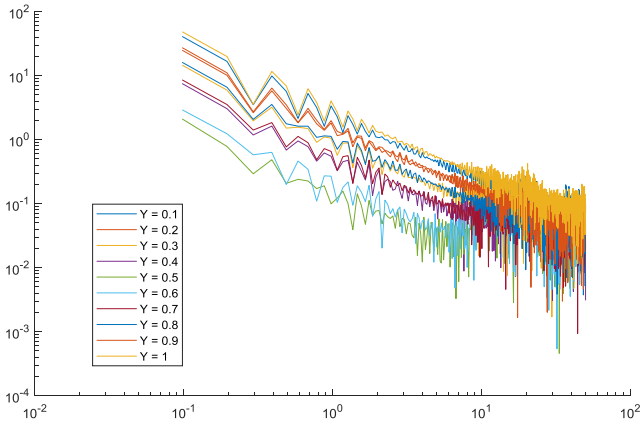

Figure 4.43 Re 100, ρ_1, ϕ = 0.5

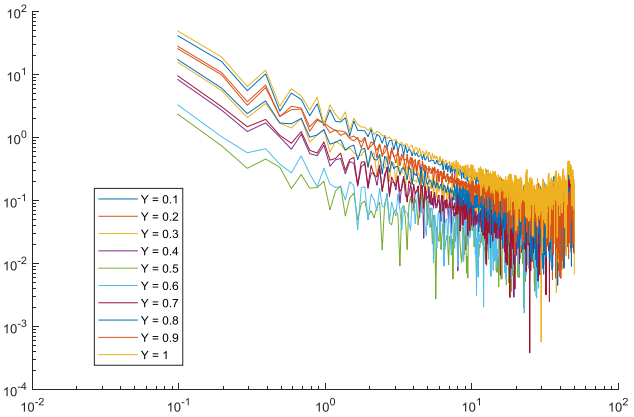

Figure 4.44 Re 400, ρ_1, ϕ = 0.5

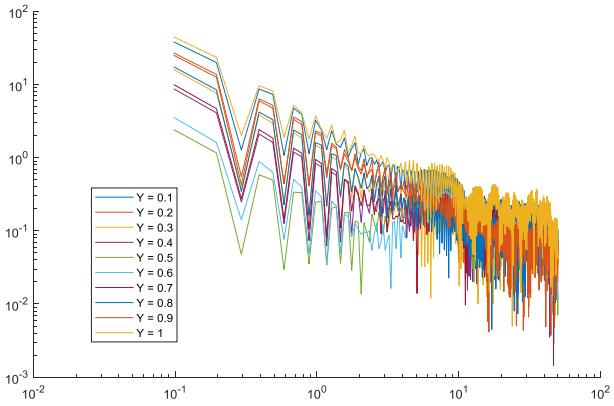

Figure 4.45 Re 1000, ρ_1, ϕ = 0.5

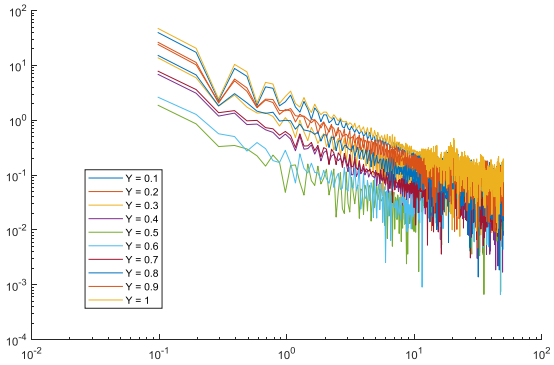

Figure 4.46 Re 100, ρ_1, ϕ = 0.75

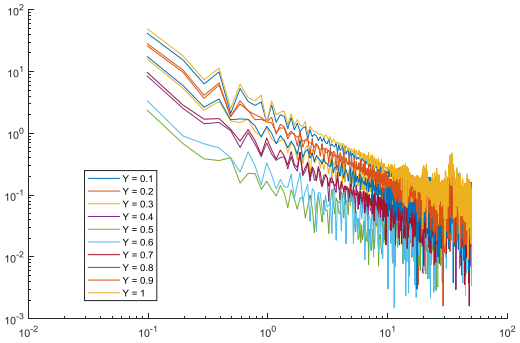

Figure 4.47 Re 400, ρ_1, ϕ = 0.75

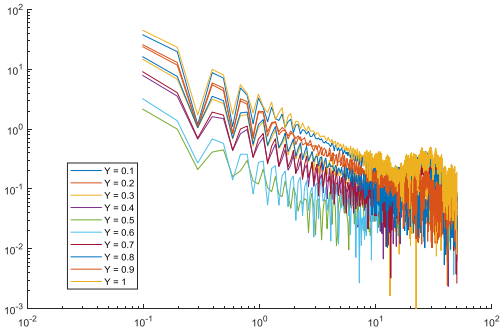

Figure 4.48 Re 1000, ρ_1, ϕ = 0.75

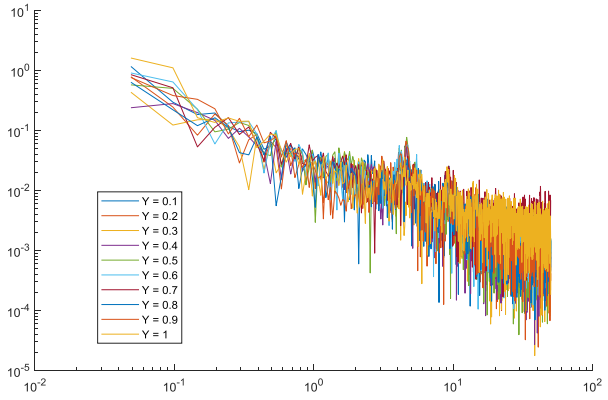

Figure 4.49 Re 100, ρ_2, ϕ = 0.25

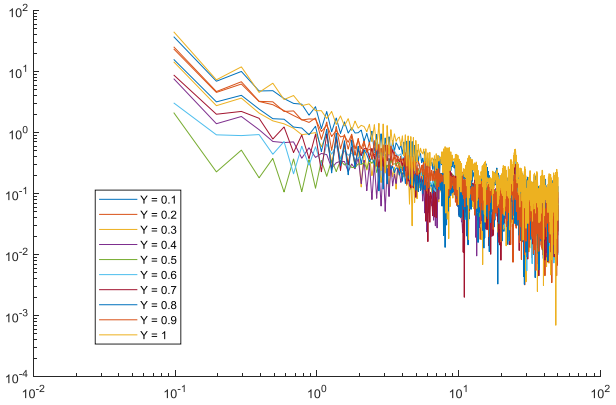

Figure 4.50 Re 400, ρ_2, ϕ = 0.25

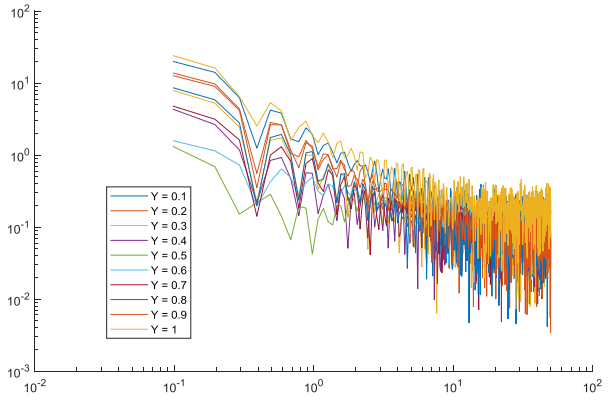

Figure 4.51 Re 1000, ρ_2, ϕ = 0.25

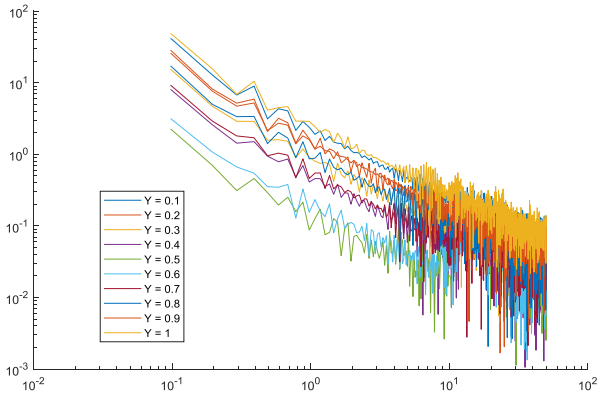

Figure 4.52 Re 100, ρ_2, ϕ = 0.5

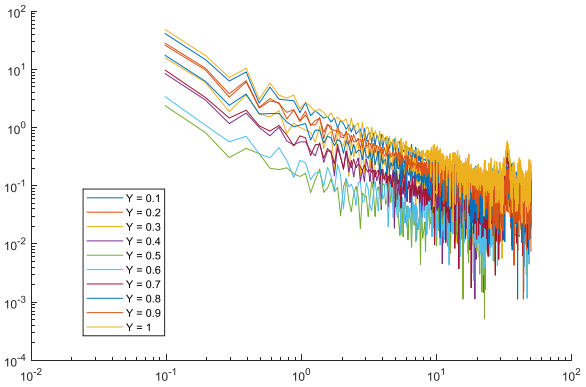

Figure 4.53 Re 400, ρ_2, ϕ = 0.5

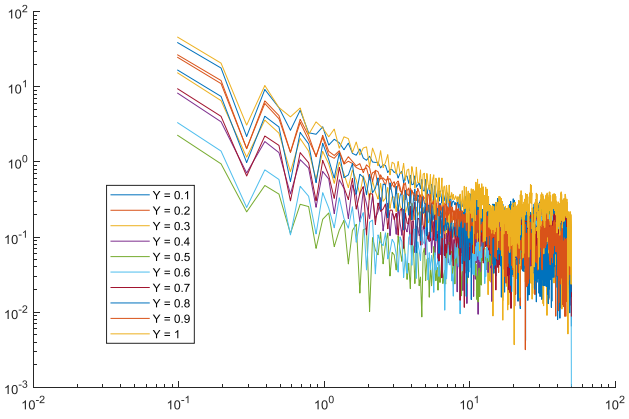

Figure 4.54 Re 1000, ρ_2, ϕ = 0.5

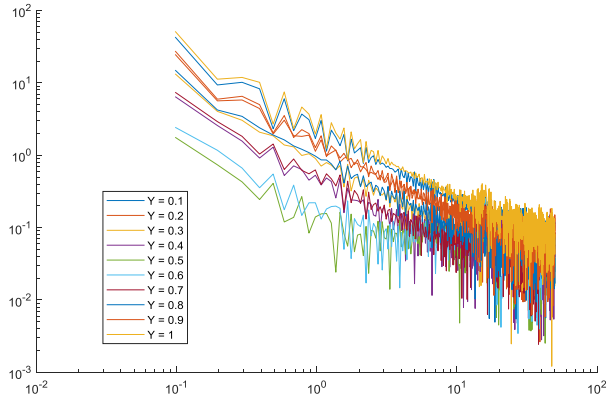

Figure 4.55 Re 100, ρ_2, ϕ = 0.75

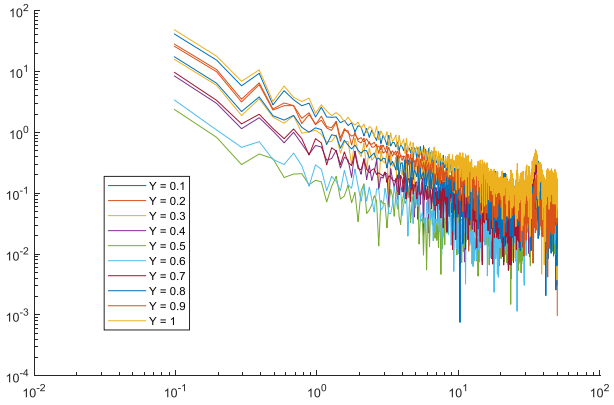

Figure 4.56 Re 400, ρ_2, ϕ = 0.75

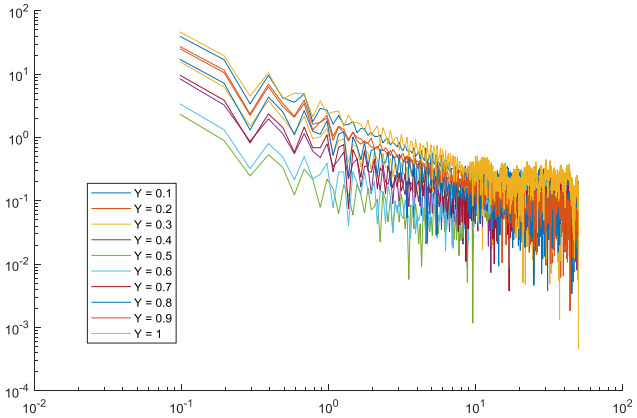

Figure 4.57 Re 1000, ρ_2, ϕ = 0.75

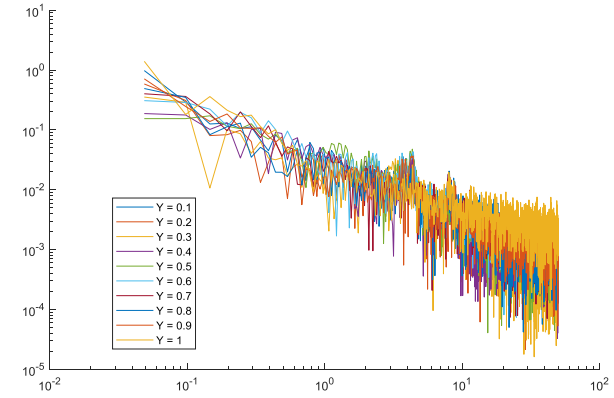

Figure 4.58 Re 100, ρ_3, ϕ = 0.25

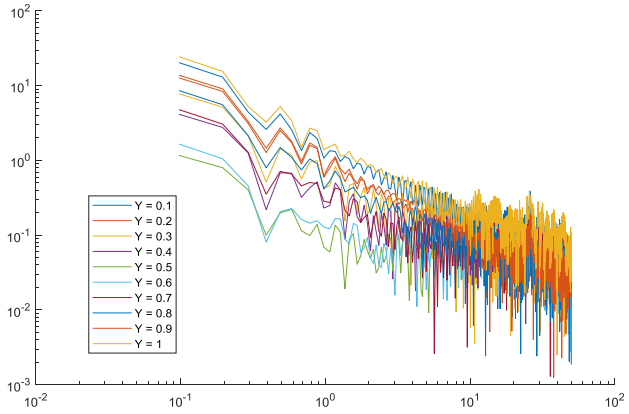

Figure 4.59 Re 400, ρ_3, ϕ = 0.25

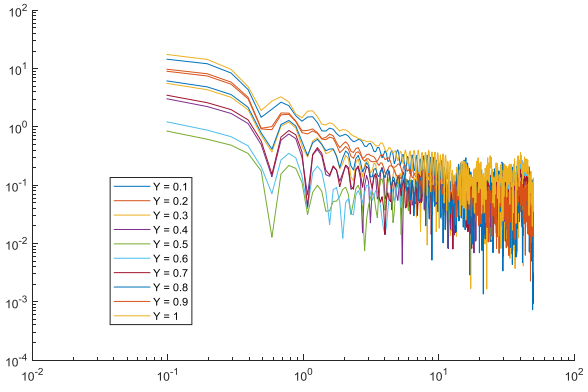

Figure 4.60 Re 1000, ρ_3, ϕ = 0.25

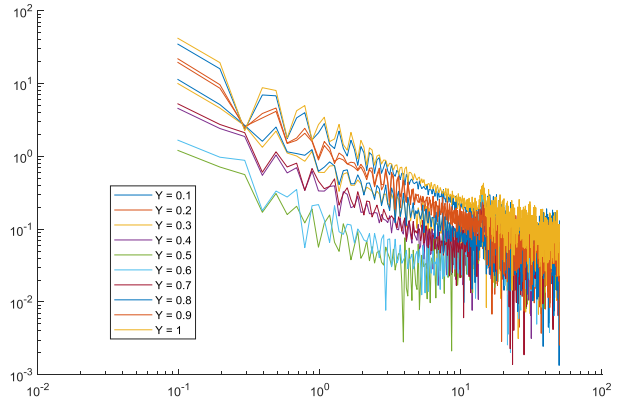

Figure 4.61 Re 100, ρ_3, ϕ = 0.5

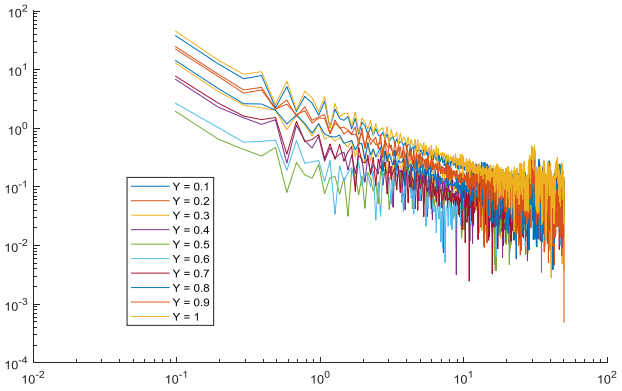

Figure 4.62 Re 400, ρ_3, ϕ = 0.5

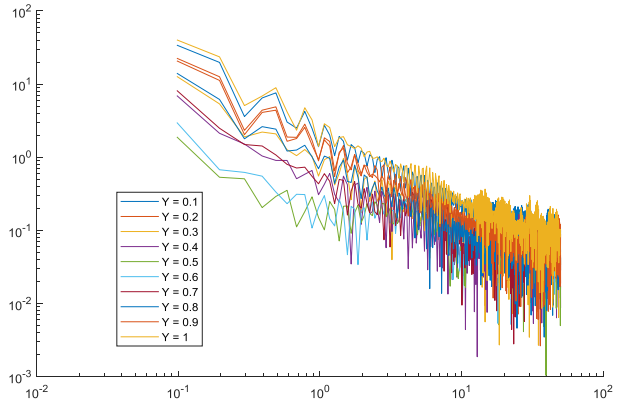

Figure 4.63 Re 1000, ρ_3, ϕ = 0.5

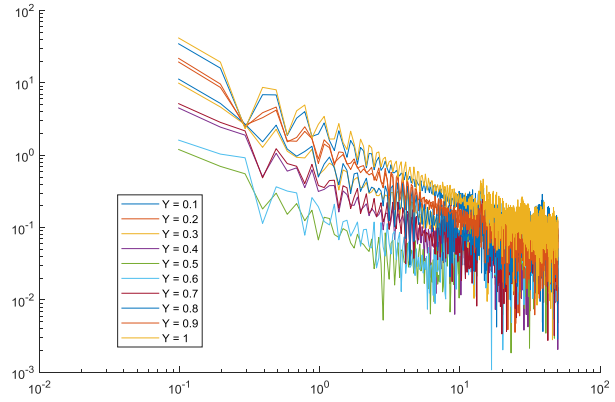

Figure 4.64 Re 100, ρ_3, ϕ = 0.75

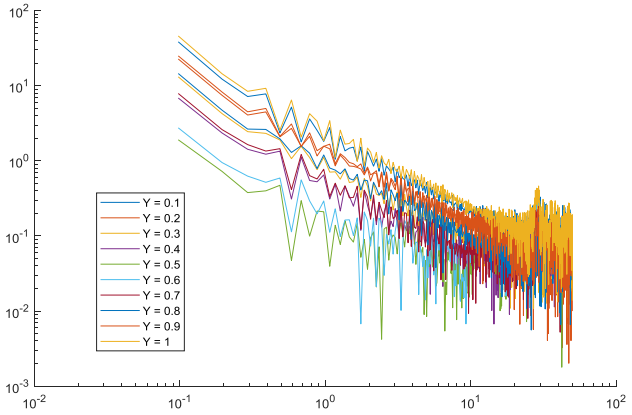

Figure 4.65 Re 400, ρ_3, ϕ = 0.75

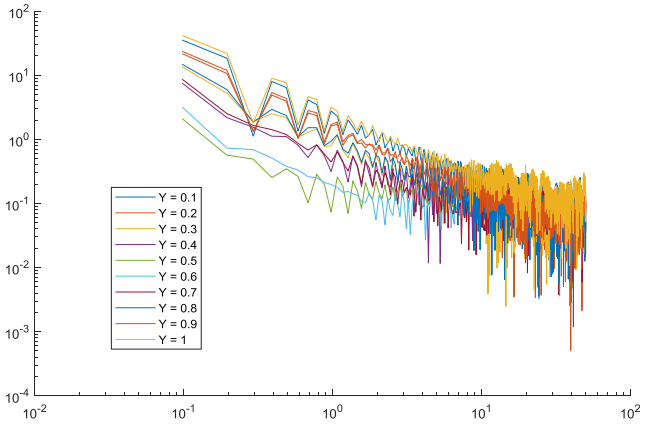

Figure 4.66 Re 1000, ρ_3, ϕ = 0.75

4.6 Flow structures

The flow characteristics in the lid driven cavity are observed through stream lines of the flow throughout the transient state and the steady state. A typical square lid-driven cavity shows a primary vortex and corner eddies which can be downstream eddy and upstream eddy depending on their direction.

With change in the aspect ratio of the lid-driven cavity from 1 to 1.5 there are some interesting changes observed in the flow structures. Unperturbed flows i.e. the lid-driven cavity flows without particles shows a primary vortex, downstream eddy and upstream eddy for Re 100 and is shown in figure 4.70. Both downstream eddy and upstream eddy in contact with each other can be observed in the figure. For Reynolds number Re400 a secondary primary vortex forming in the lower side of the cavity is seen. No formation of corner eddies i.e. downstream eddy and upstream eddy is seen. For Re1000 a primary vortex, secondary vortex and corner eddies were observed.

When the lid-driven cavity is perturbed there are three types of steady state flow structures observed.

4.6.1 One Vortex

The simulations highlighted in the Table 2, after reaching steady state show one primary vortex with no corner eddies.

Table 2: Flow structures a steady state - One vortex

$\rho_1 = \frac{\rho_p}{\rho_f} = 0.5$			
φ_1 = 25 %	Re100	Re400	Re1000
φ_2 = 50 %	Re100	Re400	Re1000
φ_3 = 75 %	Re100	Re400	Re1000
$\rho_2 = \frac{\rho_p}{\rho_f} = 1$			
φ_1 = 25 %	Re100	Re400	Re1000
φ_2 = 50 %	Re100	Re400	Re1000
φ_3 = 75 %	Re100	Re400	Re1000
$\rho_3 = \frac{\rho_p}{\rho_f} = 2$			
φ_1 = 25 %	Re100	Re400	Re1000
φ_2 = 50 %	Re100	Re400	Re1000
φ_3 = 75 %	Re100	Re400	Re1000

The perturbed flow structures of the highlighted simulations are shown in the figure 4.67. Figure 4.68 shows the flow structure of unperturbed Re400 and Re1000.

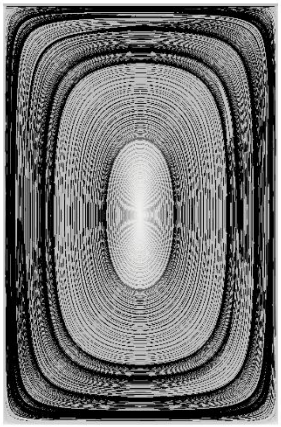

Figure 4.67 Perturbed - One vortex

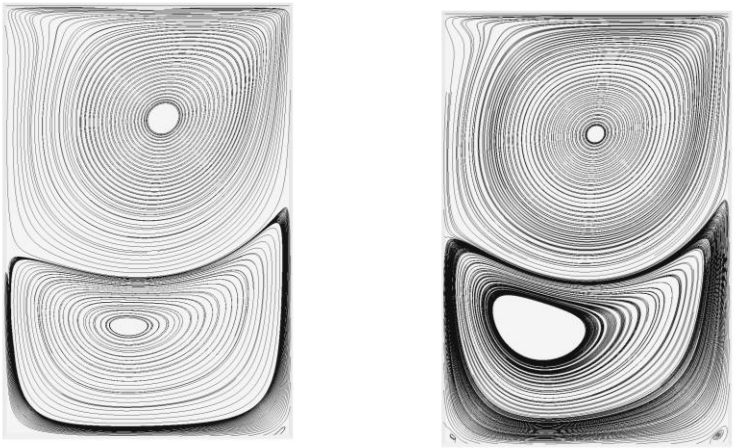

Figure 4.68 Unperturbed - One vortex

4.6.2 Two Vortices

The simulations highlighted in the Table 3, after reaching steady state show a primary vortex, secondary vortex, corner eddies and eddy between primary and secondary vortex. An interesting phenomenon is observed here. When perturbed, the flow structure of Re100 shown is figure 4.69 is very similar to unperturbed flow structure of Re1000 shown in figure 4.68, with vortices inverted.

Table 3: Flow structures a steady state - Two vortices

$\rho_1 = \frac{\rho_p}{\rho_f} = 0.5$			
φ_1 = 25 %	Re100	Re400	Re1000
φ_2 = 50 %	Re100	Re400	Re1000
φ_3 = 75 %	Re100	Re400	Re1000
$\rho_2 = \frac{\rho_p}{\rho_f} = 1$			
φ_1 = 25 %	Re100	Re400	Re1000
φ_2 = 50 %	Re100	Re400	Re1000
φ_3 = 75 %	Re100	Re400	Re1000
$\rho_3 = \frac{\rho_p}{\rho_f} = 2$			
φ_1 = 25 %	Re100	Re400	Re1000
φ_2 = 50 %	Re100	Re400	Re1000
φ_3 = 75 %	Re100	Re400	Re1000

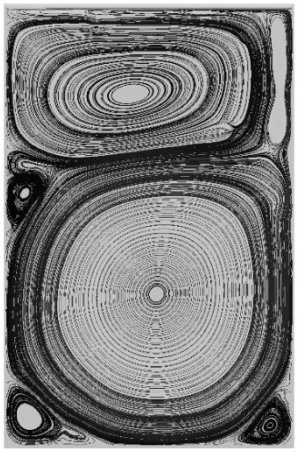

Figure 4.69 Perturbed - Two vortices

4.6.3 One vortex with corner eddies

The simulations highlighted in the Table 4, after reaching steady state show a primary vortex, and corner eddies as shown in figures 4.70 and 4.71.

Table 4: Flow structures a steady state - One vortex with corner eddies

$\rho_1 = \frac{\rho_p}{\rho_f} = 0.5$			
φ_1 = 25 %	Re100	Re400	Re1000
φ_2 = 50 %	Re100	Re400	Re1000
φ_3 = 75 %	Re100	Re400	Re1000
$\rho_2 = \frac{\rho_p}{\rho_f} = 1$			
φ_1 = 25 %	Re100	Re400	Re1000
φ_2 = 50 %	Re100	Re400	Re1000
φ_3 = 75 %	Re100	Re400	Re1000
$\rho_3 = \frac{\rho_p}{\rho_f} = 2$			
φ_1 = 25 %	Re100	Re400	Re1000
φ_2 = 50 %	Re100	Re400	Re1000
φ_3 = 75 %	Re100	Re400	Re1000

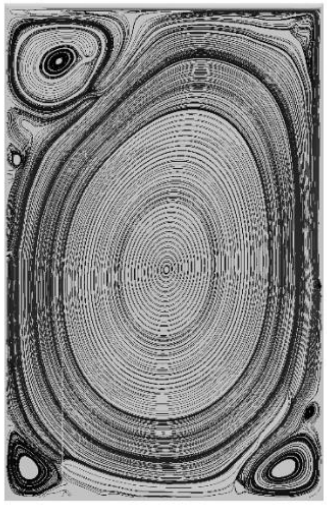

Figure 4.70 Perturbed - One vortex with corner eddies

Figure 4.71 Unperturbed - One vortex with corner eddies

5. CONCLUSIONS

- When particles are present to produce drag and particle-particle perturbations in the base flow, the primary stable flow structure is one primary vortex with no corner eddies even with different Reynolds numbers, area fractions and density ratios
- For Reynolds number = 100 and area fraction = 0.25, we have flow structures of an unperturbed flow structure at Reynolds number = 1000, but inverted.
- Of the two perturbation sources in base fluid flow, drag-induced perturbations was the more significant contributor to how the resulting flow structures developed
- At low Reynolds numbers, individual particle drag affected the time to reach a stable flow structure is most

6. REFERENCES

[1] Anil Kumar, S.P. Agrawal. "Mathematical and simulation of lid driven cavity flow at different aspect ratios using single relaxation time lattice boltzmann technique." *American Journal of Theoretical and Applied Statistics* 2 (2013): 87-93.

[2] B. H. Xu, A. B. Yu. "Numerical simulation of the gas-solid flow in a fluidized bed by combining discrete particle method with computational fluid dynamics." *Elsevier Science*

[3] Goong Chen, Qingang Xiong, Philip J. Morris, Eric G. Paterson,Alexey Sergeev and Yi-Ching Wang. *OpenFOAM forComputational FluidDynamics*. April 2014.

[4] Greenshields, Chris. *OpenFOAM User Guide*. 2 March 2015.

[5] Jasak, Hrvoje. "OpenFOAM: Open source CFD in research and industry." *International Journal of Naval Architecture and Ocean Engineering* 1.2 (2009): 89-94.

[6] O'Brien, James G. *Introduction to Fourier Transforms for Physicists*. 5 May 2008.

[7] Omari, Reyad. "CFD Simulations of Lid Driven Cavity Flow at Moderate Reynolds Number." *European Scientific Journal* 9.15 (2013).

[8] R.G. Sousa, R.J. Poole, A.M. Afonso, F.T. Pinho, P.J. Oliveira, A. Morozov, M.A. Alves. "Lid-driven cavity flow of viscoelastic liquids." *Journal of Non-Newtonian Fluid Mechanics* 234 (2016): 129-138.

[9] Ramanan, Natarajan. "Linear Stability of Lid-driven Cavity Flow." *Physics of Fluids Phys. Fluids 6.8* (1994): 2690.

[10] U. Ghia, K. N. Ghia and C. T. Shin. "High-Re Solutions for Incompressible Flow using the Navier-Stokes Equations and a Multigrid Method." *Journal of Computational Physics* (1982): 387-411.

[11] Cesarenier, Santiago Marquez Damian, Damian Ramajo and Noberto Nigro. *Numerical Analysis of Multiphase Solid-Gas Flow with Eulerian Models and Kinetic Theory Closure*. n.d.

[12] "Cutting transport." n.d. *PetroWiki.* 29 June2015.<http://petrowiki.org/Cuttings_transport>.

[13] *Computing Facilities - GAEA*. n.d. <http://niu.edu/hpc/facilities/gaea.shtml>.